PONTIFICIA UNIVERSIDAD CATÓLICA DE CHILE
FACULTAD DE FÍSICA
DEPARTAMENTO DE ASTRONOMÍA Y ASTROFÍSICA

Evolution of axially symmetric magnetic fields in neutron star crusts due to the Hall drift

by

Pablo Marchant

Tesis presentada a la Facultad de Física de la
Pontificia Universidad Católica de Chile para
el grado (académico) de Magíster en Astrofísica

Supervisor	:	Prof. Andreas Reisenegger (Pontificia U. Católica de Chile)
Co-Supervisor	:	Prof. Juan Alejandro Valdivia (U. de Chile)
Correctors	:	Prof. Jorge Cuadra (Pontificia U. Católica de Chile)
	:	Prof. Rafael Benguria (Pontificia U. Católica de Chile)

July 2012
Santiago, Chile

Acknowledgements

I would like to express my thanks to my supervisor, Andreas Reisenegger, for his very active participation and interest in the development of my thesis, and for his great impact during the last years on my general development towards becoming a professional astrophysicist. I also extend my thanks to Juan Alejandro Valdivia for his great disposition towards this work, and to whom I owe a lot of the knowledge acquired on numerical methods during this last year. Also, I would like to thank Jaime Hoyos, who provided me with results from numerical simulations that were very important to check the validity of my results, and also for being a part of the many discussions that concluded with this work.

Great thanks go of course to my family, always supporting me and lending an ear to tell them about my work and hearing patiently about subjects that many times were not even clear to me. I certainly hold my achievements as theirs.

And I would like to extend some special thanks to everyone involved in the development of astronomy programs in Chile. Thanks to all of them, I have found a life choice that enriches me daily, which I greatly enjoy (and suffer from time to time).

Finally, I want to thank all the entities involved in the funding of my studies and associated activities, including a CONICYT Scholarship for Master Studies, the CONICYT International Collaboration Grant DFG-06, the FONDECYT Regular Grant 1110213, the Basal Center for Astronomy and Associated Technologies (CATA) PFB-06/2007 and SOCHIAS.

Abstract

In neutron star crusts, the advection of magnetic field by the moving electrons, an effect known as Hall drift, should play a very important role as ions and protons should remain essentially fixed. Although Hall drift preserves the magnetic field energy, it has been argued that it may drive a turbulent cascade to scales at which Ohmic dissipation becomes effective (Goldreich and Reisenegger 1992), allowing a much faster decay in objects with very strong fields. I have developed a finite-difference code, restricted to axial symmetry, to study the evolution of magnetic fields due to Hall drift and Ohmic dissipation in a uniform spherical shell. The core of the star is assumed to be a superconductor that has expelled all magnetic flux due to the Meissner effect. For the case of constant resistivity and electron density, I have compared my code with the spectral code used by Hollerbach and Rüdiger (2002), obtaining a remarkable agreement. I also studied the stability of analytical Hall equilibria, finding that these fields decay essentially on the timescale of the fundamental Ohmic mode and thus appear to be stable to axially symmetric perturbations.

Contents

List of Figures

Chapter 1

Introduction

The usual estimation of neutron star magnetic fields is done taking into account the magnetic dipole model for pulsars. In this model, the magnetic field is taken to be a misaligned dipole with respect to the rotation axis of the star, producing dipole radiation and thus spinning down the star. By equating the rate of energy loss due to radiation and spindown (see, for instance, Shapiro and Teukolsky 1983), it can be shown that $\dot{\Omega} = -B_P^2 R^6 \Omega^3 \sin^2 \alpha / 6c^3 I$, where Ω is the angular velocity of the star, B_P is the surface magnetic field strength at the poles, R is the radius of the star, α is the inclination angle between the rotational and the magnetic axis, c is the speed of light and I is the moment of Inertia of the star. Thus, measurements of Ω and $\dot{\Omega}$ can be used to estimate B_P, which results in a very wide range of surface field strengths, going from 10^8 G up to fields that could be as large as 10^{15} G (Kaspi et al. 1999).

Most low-field objects are observed in binary systems, and their low fields are thought to be a consequence of accretion, which serves also to speed up the star's rotation (see, for instance, Bhattacharya and van den Heuvel 1991). Typical radio pulsars on the other hand are isolated objects, and if they are affected by any noticeable magnetic field evolution, it should be due to processes inherent to the neutron star and not the environment. Although it has been argued that field decay in timescales $< 10^7$ yr is required to explain the distribution of radio pulsars in the $P - \dot{P}$ diagram (Ostriker and Gunn 1969, Narayan and Ostriker 1990), others claim that such short timescales are not required (Bhattacharya et al. 1992, Faucher-Giguère and Kaspi 2006), and a clear answer is not yet established.

The introduction of magnetars, objects with surface magnetic fields of up to 10^{15}G,

which would be required to power the high X-ray luminosities of AXPs (anomalous X-ray pulsars), or the gamma ray bursts of SGRs (soft gamma repeaters) introduces a whole new level to the study of fast magnetic field evolution. Such strongly magnetic neutron stars were predicted as a plausible product of dynamo effects in the convective stages of very young and rapidly rotating neutron stars, producing internal fields in principle up to $3 \times 10^{17}(1 \text{ ms}/P_0)$ G, where P_0 is the initial period of rotation (Thompson and Duncan 1993). Unlike classical radio pulsars, magnetars emit much more energy than their rotational energy loss, requiring an additional energy reservoir. The magnetic field evolution is then expected to be of paramount importance to explain the phenomenology of these objects, be it by keeping a high temperature by dissipation of the magnetic field, forming twists in the magnetosphere which can give rise to X-rays, or causing stresses in the neutron star crust that can eventually be released in giant gamma ray bursts (Thompson and Duncan 1995, 1996, Thompson et al. 2000, 2002). For a review on the properties and theory of magnetars, see Mereghetti (2008). In order to understand in detail how these effects come into play, it is neccesary to study the mechanisms for magnetic field evolution inside the neutron star.

1.1 Hall drift and Ohmic decay

In this thesis work, I will restrict myself to magnetic field evolution in the crusts of neutron stars, ignoring possible effects involving the fluid core. In the crust, ions are locked into a crystal lattice, and the only freely moving charged species are the electrons. This electron fluid should have a negligible acceleration, which in turn implies that the Lorentz force should be equal to the time-averaged momentum loss through collisions. This yields a generalized Ohm's law,

$$\boldsymbol{j} = \sigma \left(\boldsymbol{E} + \frac{\boldsymbol{v}_e \times \boldsymbol{B}}{c} \right), \tag{1.1}$$

where σ is the electrical conductivity of the medium. Magnetic field evolution then follows from the induction equation

$$\frac{\partial \boldsymbol{B}}{\partial t} = -c\nabla \times \boldsymbol{E}, \tag{1.2}$$

$$= \nabla \times \left(\boldsymbol{v}_e \times \boldsymbol{B} - \tfrac{c\boldsymbol{j}}{\sigma} \right), \tag{1.3}$$

where the first term in the last expression describes advection of field lines by the electron fluid. In the limit of slowly varying fields, the displacement current can be ignored, and Ampères law $\boldsymbol{j} = \frac{c}{4\pi}\nabla \times \boldsymbol{B}$ is valid. Since the current density is simply $-en_e\boldsymbol{v}_e$ (where n is the electron density), Eq. (1.3) becomes

$$\frac{\partial \boldsymbol{B}}{\partial t} = -\nabla \times \left(\frac{c}{4\pi n e}[\nabla \times \boldsymbol{B}] \times \boldsymbol{B} + \eta \nabla \times \boldsymbol{B} \right), \tag{1.4}$$

where $\eta \equiv c^2/(4\pi\sigma)$ is the magnetic diffusivity. A more general expression than this, which includes also the motions of protons and has this result as a limiting case, is given by Goldreich and Reisenegger (1992). That general case can be used to describe magnetic field evolution in the core of the star, where protons are mobile. For simplicity, I will consider both n and η to be functions only of the radial coordinate r, and time independent, which is not correct if the evolution of the star's temperature is taken into account (Cumming et al. 2004, Pons et al. 2009). This equation contains two different effects that act on two distinct timescales, which can be estimated as

$$t_{Hall} \equiv \frac{4\pi n_0 e R^2}{cB_0}, \quad t_{Ohm} \equiv \frac{R^2}{\eta_0}, \tag{1.5}$$

where characteristic values B_0 for the magnetic field, n_0 for n, η_0 for η, and the radius of the star R for the radial coordinate r are used. The ratio of these two quantities defines the so-called magnetization parameter R_B (a close analog to the Reynolds number of fluid mechanics),

$$R_B = \frac{t_{Ohm}}{t_{Hall}} = \frac{cB_0}{4\pi\eta_0 n_0 e}. \tag{1.6}$$

An estimate for these two timescales associated to a characteristic length scale L instead of the whole radius of the star was given by Goldreich and Reisenegger (1992),

$$t_{Hall} \simeq 5 \times 10^8 \frac{L_5^2}{B_{12}} \left(\frac{\rho}{\rho_{nuc}} \right) \text{ yr}, \qquad t_{Ohm} \simeq 2 \times 10^{11} \frac{L_5^2}{T_8^2} \left(\frac{\rho}{\rho_{nuc}} \right)^3 \text{ yr}, \tag{1.7}$$

where $L_5 = L/(10^5 \text{ cm})$, T_8 is the temperature in units of 10^8 K, ρ is the mass density, $\rho_{nuc} = 2.8 \times 10^{14}$ gr cm^3 and B_{12} is the magnetic field measured in units of 10^{12} G. This suggests that magnetar-like fields could evolve via Hall drift on timescales of the order of Myr or even less[1]. However, as shown in Goldreich and Reisenegger (1992), Hall drift is a conservative effect, and thus cannot produce a decay of the magnetic energy by itself. The mechanism of evolution through Hall drift was first proposed by Jones (1988), who hypothesized that this effect could transport flux towards the outer regions of the crust, where Ohmic dissipation is much more efficient than in the inner regions. Goldreich and Reisenegger (1992), on the other hand, proposed that Hall drift would cause a turbulent cascade, driving the field to structures of small spatial scales at which Ohmic dissipation can become effective. Vainshtein et al. (2000) constructed a plane-parallel model with an electron density that varies with depth and a purely horizontal field, showing that the evolution through Hall drift is governed by Burgers' equation, which develops strong discontinuities corresponding to current sheets. The inclusion of Ohmic dissipation results in rapid decay of magnetic energy in these regions. Reisenegger et al. (2007) extended this result to the case of a purely toroidal (azimuthal) and axially symmetric magnetic field, showing in this case that the evolution through Hall drift can again be described with Burgers' equation. Although these analytical developments are a big step forward to understand the evolution of the magnetic field, a full understanding of this process seems to require the use of numerical simulations due to the complex non-linear character of Eq. (1.3).

1.2 Numerical simulations of Hall drift in neutron stars

Various authors have worked performing numerical simulations to solve Eq. (1.3). Urpin and Shalybkov (1991) performed simulations of a purely toroidal field on a model star with

[1] 1 Myr = 10^6 years

constant (both in space and time) electron density and resistivity, showing that a field of a single polarity drifts parallel to the axis of symmetry towards one of the hemispheres, developing a current sheet just below the surface, and thus inducing a rapid dissipation of magnetic energy. Shalybkov and Urpin (1997) managed to perform a simulation for an initially purely poloidal field in a conducting sphere for a magnetization parameter up to $R_B = 100$. They showed that a toroidal component develops, and the poloidal and toroidal components then transfer energy between each other with a clear periodic behavior that has an increasing period as the field intensity decays. In this case, an evolution towards very small length scales was not observed.

Hollerbach and Rüdiger (2002) used a spectral code to solve for combinations of fundamental Ohmic decay modes restricted to a spherical shell that represents the neutron star crust, under the assumption of constant electron density and resistivity, testing fields with dominant poloidal components. They observed periodic oscillations just as was the case with Shalybkov and Urpin (1997). However, they could not push their code beyond $R_B = 200$, which is still far from the values up to $R_B = 1000$ that can be reached in the innermost regions of neutron star crusts (Cumming et al. 2004). Moreover, as R_B increases, current sheets are more likely to form, which will probably be problematic for a spectral code to cope with. Hollerbach and Rüdiger (2004) extended this work to a simplified model of a stratified star and tested a purely toroidal field in order to compare their results with the analytical calculation of Vainshtein et al. (2000). Their results show for this purely toroidal field that strong current sheets are in fact produced, with the time for energy decay scaling with the Hall timescale rather than the Ohm timescale. However, they also showed that the inclusion of a small poloidal component, even if it is much weaker than the toroidal component, significantly affects the evolution by inhibiting the formation of very strong discontinuities.

Geppert and Pons (2007) also performed simulations of the combined effect of Hall drift and Ohmic decay, using realistic (but time-independent, as they did not consider thermal evolution) models for the electron density and the resistivity, showing that fields with typical strengths of 10^{14} G can have a Hall-dominated phase of evolution with rapid Ohmic decay that lasts between 10^3 and 10^4 years. Moreover, they also saw that stratification favors drift of the toroidal field towards the interior, where conductivity is much higher, reaching in the end stable configurations with lifetimes of the order of 10^6 years. More recently, Pons et al. (2009) successfully performed simulations of both the magnetic and

the thermal evolution of a neutron star, with the magnetic field acting as an additional heating source. These simulations though considered only the effect of Ohmic decay, and did not take Hall drift into account. They saw that the interplay between the two effects is of vital importance for high field ($> 10^{13}$ G) neutron stars, for which a high temperature and low conductivity are mantained at the initial stages of the evolution, reaching similar field strengths of about $2 - 3 \times 10^{13}$ G at later stages, independent of the initial field strength. Both of these works used a code that worked with finite-differences in the radial direction and a spectral decomposition in the latitudinal direction.

All the simulations described however, are restricted to axial symmetry, and its hard to assess precisely what the impact of a full 3D simulation would be, and how much of the results already obtained would still apply.

The purpose of this thesis has been to develop a finite-difference code to time evolve Eq. (1.3), in order to test some simple scenarios of magnetic field evolution, trying to better assess general properties of the Hall drift term in the induction equation. In particular, I am interested in Hall equilibria and their stability, as the possible existence of stable fields with quiescent evolution could have an important impact on the general properties and evolution scenarios of highly magnetized neutron stars. The code developed is also intended to serve as a basis for future work focused on achieving a better understanding of magnetic field evolution in both crust and core of neutron stars. Chapter 2 describes the mathematical framework used for the simulations. Chapter 3 describes the numerical methods used and a couple of test cases that were simulated with the developed code. Chapter 4 studies two different situations, first, the different evolution of either poloidally or toroidally dominated fields, and second, the stability of an analytically known Hall equilibrium. Finally, Chapter 5 presents the conclusions of my work.

Chapter 2

Axially symmetric fields

For the purpose of this thesis, I restrict myself to axially symmetric fields, in which case $\boldsymbol{B}$ can be written in terms of two scalar functions as

$$\boldsymbol{B} = \nabla\alpha(r,\theta) \times \nabla\phi + \beta\nabla\phi, \tag{2.1}$$

where ϕ is the azimuthal angle in spherical coordinates. Thus, $\alpha(r,\theta)$ describes the poloidal field and $\beta(r,\theta)$ the toroidal field. The curl of $\boldsymbol{B}$ can be expressed in terms of these functions as

$$\nabla \times \boldsymbol{B} = -\Delta^*\alpha\nabla\phi + \nabla\beta \times \nabla\phi, \tag{2.2}$$

where Δ^* is called the Grad-Shafranov operator and is defined as

$$\Delta^* \equiv= \varpi^2\nabla\cdot(\varpi^{-2}\nabla) = \partial_r^2 + \frac{\sin\theta}{r^2}\partial_\theta\left(\frac{\partial_\theta}{\sin\theta}\right), \tag{2.3}$$

where $\varpi \equiv r\sin\theta$ is the radial cylindrical coordinate. Using this, and defining $\chi \equiv c/(4\pi e n \varpi^2)$, eq. (1.4) gives

$$\begin{aligned}\nabla\left(\frac{\partial\alpha}{\partial t}\right) \times \nabla\phi + \frac{\partial\beta}{\partial t}\nabla\phi = \\ \nabla \times \left(\varpi^2\chi[\Delta^*\alpha\nabla\phi - \nabla\beta\times\nabla\phi] \times [\nabla\alpha\times\nabla\phi + \beta\nabla\phi] - \eta[-\Delta^*\alpha\nabla\phi + \nabla\beta\times\nabla\phi]\right).\end{aligned} \tag{2.4}$$

After expanding the cross product inside the curl, each term in this equation is either poloidal or toroidal. Taking this into account, I have two equations which together are equivalent to the previous one,

$$\begin{aligned}\nabla\left(\frac{\partial\alpha}{\partial t}\right)\times\nabla\phi =&\nabla\times\left(\varpi^2\chi[\nabla\beta\times\nabla\phi]\times[\nabla\alpha\times\nabla\phi]+\eta\Delta^*\alpha\nabla\phi\right),\\ \frac{\partial\beta}{\partial t}\nabla\phi =&\nabla\times\left(\varpi^2\chi\Delta^*\alpha\nabla\phi\times[\nabla\alpha\times\nabla\phi]+\varpi^2\chi\beta\nabla\phi\times[\nabla\beta\times\nabla\phi]-\eta\nabla\beta\times\nabla\phi\right).\end{aligned} \tag{2.5}$$

These equations can be transformed into equations for the time derivatives of the scalar functions α and β,

$$\begin{aligned}\frac{\partial\alpha}{\partial t} =&\varpi^2\chi[\nabla\alpha\times\nabla\beta]\cdot\nabla\phi+\eta\Delta^*\alpha\\ \frac{\partial\beta}{\partial t} =&\varpi^2(\nabla[\chi\Delta^*\alpha]\times\nabla\alpha+\beta\nabla\chi\times\nabla\beta)\cdot\nabla\phi+\varpi^2\nabla\cdot\left(\frac{\eta\nabla\beta}{\varpi^2}\right).\end{aligned} \tag{2.6}$$

Using t_{Hall} as the unit of time and expressing everything in terms of the characteristic values B_0, n_0, η_0, and the radius of the star, the equations for α and β can be written in a dimensionless form, namely,

$$\begin{aligned}\frac{\partial\alpha}{\partial t} =&\varpi^2\chi[\nabla\alpha\times\nabla\beta]\cdot\nabla\phi+R_B^{-1}\eta\Delta^*\alpha\\ \frac{\partial\beta}{\partial t} =&\varpi^2(\nabla[\chi\Delta^*\alpha]\times\nabla\alpha+\beta\nabla\chi\times\nabla\beta)\cdot\nabla\phi+R_B^{-1}\varpi^2\nabla\cdot\left(\frac{\eta\nabla\beta}{\varpi^2}\right),\end{aligned} \tag{2.7}$$

where the dimensionless χ is given by $\chi = 1/(\varpi^2 n)$, of course with ϖ and n in their dimensionless versions. Two important points which are apparent from eqs. (2.7) should be noted:

- A purely toroidal field remains toroidal.
- A purely poloidal field will immediately produce a toroidal component unless the Hall term is exactly equal to zero.

The equation for β can be rewritten in conservative form,

$$\frac{1}{\varpi^2}\frac{\partial\beta}{\partial t} = \nabla\times(\chi\Delta^*\alpha\nabla\alpha+\chi\beta\nabla\beta)\cdot\nabla\phi+R_B^{-1}\nabla\cdot\left(\tfrac{\eta\nabla\beta}{\varpi^2}\right) \tag{2.8}$$

$$= \nabla\cdot\left(\nabla\phi\times[\chi\Delta^*\alpha\nabla\alpha+\chi\beta\nabla\beta]+R_B^{-1}\tfrac{\eta\nabla\beta}{\varpi^2}\right), \tag{2.9}$$

from where it can be seen that the quantity

$$I_1 = \int_V \frac{\beta}{\varpi^2}\,\mathrm{d}\,V = 2\pi \int_0^\pi \int_0^R B_{tor} r\,\mathrm{d}\,r\,\mathrm{d}\,\theta, \tag{2.10}$$

which is (except for a constant) the magnetic flux crossing a halfplane limited by the symmetry axis, should be conserved except for losses at the boundaries.

For the implementation of the numerical simulations, the star is considered to be perfectly spherical, so I use eqs. (2.7) in spherical coordinates,

$$\begin{aligned}\frac{\partial}{\partial t}\left(\frac{\beta}{\sin\theta}\right) =& \frac{\partial}{\partial r}\left(\chi\Delta^*\alpha\frac{\partial\alpha}{\partial\theta} + \chi\beta\frac{\partial\beta}{\partial\theta} + R_B^{-1}\frac{\eta}{\sin\theta}\frac{\partial\beta}{\partial r}\right) \\ &+ \frac{\partial}{\partial\theta}\left(-\chi\Delta^*\alpha\frac{\partial\alpha}{\partial r} - \chi\beta\frac{\partial\beta}{\partial r} + R_B^{-1}\frac{\eta}{r^2\sin\theta}\frac{\partial\beta}{\partial\theta}\right) \\ \frac{\partial\alpha}{\partial t} =& \sin\theta\chi\left(\frac{\partial\beta}{\partial\theta}\frac{\partial\alpha}{\partial r} - \frac{\partial\beta}{\partial r}\frac{\partial\alpha}{\partial\theta}\right) + R_B^{-1}\eta\Delta^*\alpha.\end{aligned} \tag{2.11}$$

An important property should be noted about some of the symmetries related to these two equations. First, if α is either symmetric or antisymmetric with respect to the equator, it is straightforward to show that $\Delta^*\alpha$ preserves that symmetry. Then, if η and n depend only on the radial coordinate, and α and β are respectively symmetric and antisymmetric with respect to the equator, Eq. (2.11) implies that $\partial\alpha/\partial t$ will be symmetric with respect to the equator, and $\partial\beta/\partial t$ will be antisymmetric, so the initial symmetries are preserved. The initial symmetries will also be preserved if α and β are both antisymmetric with respect to the equator. However, if β is symmetric with respect to the equator, the Hall term for $\partial\beta/\partial t$ will have antisymmetric terms, so the initial symmetry will be broken. These properties have already been noted by Hollerbach and Rüdiger (2002).

2.1 Boundary conditions

For the simulations, I consider the magnetic field to be present only at the crust and the exterior of the neutron star. The core of the star is (for now) considered to be a superconducting fluid which has completely expelled all its magnetic flux due to the Meissner effect, and the radius of the crust-core interface is defined as r_{min}.

2.1.1 Conditions at the axis ($\theta = 0, \pi$)

The only requirement at the axis is that the magnetic field is a single-valued function. This implies that $B_\phi = B_\theta = 0$, which in turn gives

$$\beta(\theta = 0, \pi) = 0, \qquad \frac{\partial \alpha}{\partial r}(\theta = 0, \pi) = 0, \tag{2.12}$$

which means α is constant along the axis. Since α has an arbitrary "zero-point", I choose $\alpha = 0$ at the axis.

2.1.2 Conditions at the crust-core boundary ($r = r_{min}$)

At the interface between the solid crust and the fluid core, I require the normal component of the magnetic field and the tangential component of the electric field to be continuous,

$$B_r|_{in} = B_r|_{out}, \qquad E_\theta|_{in} = E_\theta|_{out}, \qquad E_\phi|_{in} = E_\phi|_{out}, \tag{2.13}$$

Assuming (for simplicity) that the core is a superconductor with a perfect Meissner effect, the magnetic and electric fields in it are zero, and thus these conditions are simply

$$B_r(r = r_{min}) = 0, \qquad E_\theta(r = r_{min}) = 0, \qquad E_\phi(r = r_{min}) = 0. \tag{2.14}$$

The easiest of these three to apply is the first one. Since $B_r \propto \partial\alpha/\partial\theta$, it implies that α is constant at the boundary, and since I already fixed $\alpha = 0$ on the symmetry axis I must have $\alpha = 0$ at $r = r_{min}$ also.

The condition on the electric field produces a much more complex boundary condition. In terms of the magnetic field, the electric field in the crust is given by

$$-c\boldsymbol{E} = \frac{c}{4\pi n e}(\nabla \times \boldsymbol{B}) \times \boldsymbol{B} + \eta \nabla \times \boldsymbol{B}, \tag{2.15}$$

(see eq. (1.1)) so requiring the tangential component of the electric field to be zero at the boundary is equivalent to

$$0 = \left[\varpi^2 \chi (\nabla \times \boldsymbol{B}) \times \boldsymbol{B} + \eta R_B^{-1} \nabla \times \boldsymbol{B}\right]_T, \tag{2.16}$$

where T denotes the tangential component, and ϖ, χ and η are written in their dimen-

sionless forms. In terms of α and β, this produces the following two (non-linear) boundary conditions in spherical coordinates

$$\begin{aligned} 0 =& \chi\beta\frac{\partial\beta}{\partial\theta} + R_B^{-1}\frac{\eta}{\sin\theta}\frac{\partial\beta}{\partial r} \\ 0 =& \sin\theta\chi\frac{\partial\beta}{\partial\theta}\frac{\partial\alpha}{\partial r} + R_B^{-1}\eta\Delta^*\alpha, \end{aligned} \tag{2.17}$$

where it has been explicitly used that $\alpha(r_{min}, \theta) = 0$. These conditions have been written in a form that closely resembles the terms in eqs. (2.11). Using these similarities, it can be easily seen that these conditions imply that the time derivative of α is zero at the inner boundary, and that no toroidal magnetic flux is lost to the core of the star.

In order to compare my simulations with those of Hollerbach and Rüdiger (2002) and Kojima and Kisaka (2012), I consider not only these boundary conditions, but also "zero boundary conditions" where both $\alpha = 0$ and $\beta = 0$ are forced at the inner boundary. This approximation is usually justified by saying that R_B is a large number for high field neutron stars, so the resistive terms in eqs. (2.17) are negligible.

2.1.3 Conditions at the stellar surface ($r = R$)

If outside the star I consider a perfect vacuum, then the magnetic field there is completely determined by its radial component at the surface of the star, which must be continuous. Furthermore, I expect surface currents to dissipate on timescales much smaller than those of interest to us, so not only the radial component of the magnetic field must be continuous, but the tangential one also.

The condition imposed on β because of this is trivial. Since there are no currents outside the star, I must have $\beta = 0$ there, and the continuity of the azimuthal component of the field immediately gives $\beta = 0$ as a boundary condition at $r = R$.

The condition on α is much more complex, as it is non-local. As shown in Marchant et al. (2011), the continuity of the radial component of the magnetic field implies that the

field outside the star is given by

$$\begin{aligned} \boldsymbol{B} = \nabla\Psi, \quad \Psi(r,\theta,\phi) &= \sum_{l=1}^{\infty}\sum_{m=-l}^{l}\frac{a_{lm}}{r^{l+1}}Y_{lm}(\theta,\phi), \\ a_{lm} &= -\frac{R^{l+2}}{l+1}\int_{4\pi}(B_r)_{r=R}Y^*_{lm}\,\mathrm{d}\,\Omega, \end{aligned} \tag{2.18}$$

where $(B_r)_{r=R}$ is the radial field $\boldsymbol{B}\cdot\hat{\boldsymbol{r}}$ at the surface of the star, which can be expressed in terms of α as $([r^2\sin\theta]^{-1}\partial\alpha/\partial\theta)_{r=R}$. Under axial symmetry, only the coefficients with $m = 0$ are non-zero, and for these cases I have (omitting the unnecessary $m = 0$ subscript)

$$a_l = -\frac{R^{l+2}}{l+1}\int_0^{2\pi}\mathrm{d}\,\phi\int_0^{\pi}([r^2\sin\theta]^{-1}\partial\alpha/\partial\theta)_{r=R}Y^*_{l,0}\sin\theta\,\mathrm{d}\,\theta \tag{2.19}$$

$$= -\frac{R^l}{l+1}\sqrt{\frac{2l+1}{4\pi}}\cdot 2\pi\int_0^{\pi}P_l(\cos\theta)\left(\frac{\partial\alpha}{\partial\theta}\right)_{r=R}\mathrm{d}\,\theta. \tag{2.20}$$

This can be rearranged using integration by parts to obtain an integral that does not depend on the θ derivative of α. Boundary terms are zero, since I set $\alpha = 0$ at the axis and the Legendre polynomials are non-singular, so I have

$$a_l = \frac{R^l}{l+1}\sqrt{\pi(2l+1)}\int_0^{\pi}\frac{\partial P_l(\cos\theta)}{\partial\theta}\alpha(R,\theta)\,\mathrm{d}\,\theta \tag{2.21}$$

The derivative of the Legendre polynomial is simply the associated Legendre polynomial $P_l^1(\cos\theta)$, so the a_l can be solved as

$$a_l = \frac{R^l}{l+1}\sqrt{\pi(2l+1)}\int_0^{\pi}P_l^1(\cos\theta)\alpha(R,\theta)\,\mathrm{d}\,\theta = \frac{R^l}{l+1}\sqrt{\pi(2l+1)}A_l, \tag{2.22}$$

where A_l stands for the integral. This selection of the a_l coefficients will give a continuous radial component of the magnetic field, but so far I have not imposed continuity on the θ component of the field. Equating the value of B_θ just inside the star, as given by α, and just outside the star, as given by the combination of the a_l, I have

$$(B_\theta)_{r=R} = \sum_{l=1}^{\infty}\frac{a_l}{R^{l+2}}\sqrt{\frac{2l+1}{4\pi}}\frac{\partial}{\partial\theta}P_l(\cos\theta) = -\frac{1}{R\sin\theta}\left[\frac{\partial\alpha}{\partial r}\right]_{r=R}. \tag{2.23}$$

Solving for $\partial\alpha/\partial r$ at the surface, I have the boundary condition required for the continuity of the θ component of the field,

$$\left[\frac{\partial\alpha}{\partial r}\right]_{r=R} = -\sum_{l=1}^{\infty} \frac{a_l}{R^{l+1}}\sqrt{\frac{2l+1}{4\pi}}\sin\theta P_l^1(\cos\theta), \tag{2.24}$$

with a_l given by Eq. (2.22).

Another related calculation that turns out to be useful is that of the energy of the external field, expressed as a sum over the energy of the individual multipoles. Using Eq. (2.18), I have that the external magnetic energy is

$$E_{ext} \equiv \int_{r>R} \frac{\boldsymbol{B}^2}{8\pi}\,\mathrm{d}\,V = \int_{r>R} \frac{\nabla\cdot(\Psi\nabla\Psi)}{8\pi}\,\mathrm{d}\,V = \frac{1}{8\pi}\oint_S \Psi\nabla\Psi\cdot\,\mathrm{d}\,\boldsymbol{A}, \tag{2.25}$$

where S is a the surface of the star with its normal pointing towards the center[1]. Because of this, $\nabla\Psi\cdot\,\mathrm{d}\,\boldsymbol{A} = -R^2(B_r)_{r=R}\,\mathrm{d}\,\Omega$, and using the expansion of Ψ in terms of the a_{lm} of Eq. (2.18) gives me

$$E_{ext} = -\frac{1}{8\pi}\int_{4\pi}\sum_{l=1}^{\infty}\sum_{m=-l}^{l}\frac{a_{lm}}{R^{l-1}}(B_r)_{r=R}Y_{lm}(\theta,\phi)\,\mathrm{d}\,\Omega = \frac{1}{8\pi}\sum_{l=1}^{\infty}\sum_{m=-l}^{l}\frac{(l+1)|a_{lm}|^2}{R^{2l+1}}, \tag{2.26}$$

where each term in the sum is the energy associated to the corresponding multipole. Of course, under the assumption of axial simmetry, the only nonzero terms in this sum are those with $m = 0$.

2.2 Ohmic modes

The simplest part of eqs. (2.11) is the linear one given by the Ohm terms. I want to know precisely what are the decay timescales and the structure for the first eigenmodes of the evolution due solely to Ohmic decay, as these play an important role in determining how the relative intensities of the poloidal and toroidal components will evolve in the long run, and also constitute an essential test to my numerical simulations. For the purposes of this thesis, I only work with models of constant (both in time and space) resistivity, so, taking

[1] As was shown in Marchant et al. (2011), the term corresponding to the surface at infinity vanishes

this into account, eqs. (2.11) can be rewritten without the nonlinear Hall terms as

$$\frac{\partial \alpha}{\partial t} = R_B^{-1}\Delta^*\alpha, \quad \frac{\partial \beta}{\partial t} = R_B^{-1}\Delta^*\beta, \tag{2.27}$$

for which separable axially symmetric solutions can be readily obtained,

$$\alpha(r,\theta,t) = r\left[Aj_l\left(kr\right) + By_l\left(kr\right)\right]P_l^1(\cos\theta)\sin\theta e^{-t/\tau}, \tag{2.28}$$

$$\beta(r,\theta,t) = r\left[Cj_l\left(kr\right) + Dy_l\left(kr\right)\right]P_l^1(\cos\theta)\sin\theta e^{-t/\tau}, \tag{2.29}$$

where j_l and y_l are the spherical Bessel functions of order l. Also, $k \equiv (\tau R_B^{-1})^{-1/2}$, and the decay timescales τ and the ratios A/B and C/D depend on the boundary conditions used for α and β.

Outside the star there will be no currents, so the function α must satisfy $\Delta^*\alpha = 0$, and the separable solutions in this case are of the form

$$\alpha = \frac{E}{r^l}P_l^1(\cos\theta)\sin\theta, \tag{2.30}$$

where E is fixed in terms of the boundary conditions at the surface. In this case, I require continuity of both the radial and the angular derivatives of α at $r = 1$ (the surface in dimensionless coordinates), where the latter of these conditions is equivalent to demanding continuity of α through the surface. The third boundary condition is that $\alpha(r_{min}) = 0$, so the field does not pierce the superconducting core. Writing this, I have for the continuity of α across the surface

$$Aj_l\left(k\right) + By_l\left(k\right) = E, \tag{2.31}$$

for the continuity of the radial derivative at the surface

$$Aj_l\left(k\right) + By_l\left(k\right) + Akj_l'\left(k\right) + Bky_l'\left(k\right) = -lE \tag{2.32}$$

and for the zero boundary condition at r_{min}

$$Aj_l\left(kr_{min}\right) + By_l\left(kr_{min}\right) = 0. \tag{2.33}$$

These three preceding equations can be converted into a transcendental equation for k and

an equation for the ratio A/B (the value of E is irrelevant to us),

$$\begin{gathered}\left[y_l'(k)j_l(kr_{min}) - y_l(kr_{min})j_l'(k)\right] + \frac{(l+1)}{k}\left[y_l(k)j_l(kr_{min}) - y_l(kr_{min})j_l(k)\right] = 0 \\ \frac{A}{B} = -\frac{y_l(kr_{min})}{j_l(kr_{min})}.\end{gathered} \tag{2.34}$$

The different solutions of the transcendental equation will give the different radial modes for each multipole.

For the toroidal field I have two possibilities, depending on the use of zero or Meissner boundary conditions, so I deal with each of these cases separately.

- Zero BC: In this case I simply have the zero boundary condition at the surface,

$$Cj_l(k) + Dy_l(k) = 0, \tag{2.35}$$

  and the zero boundary condition at the inner radius,

$$Cj_l(kr_{min}) + Dy_l(kr_{min}) = 0. \tag{2.36}$$

  Just as with the poloidal field, these two equations can be combined into a transcendental equation for k and another one for the ratio C/D,

$$\begin{gathered}j_l(k)y_l(kr_{min}) - j_l(kr_{min})y_l(k) = 0 \\ \frac{C}{D} = -\frac{y_l(k)}{j_l(k)}.\end{gathered} \tag{2.37}$$

- Meissner BC: In this case I also have the zero boundary condition (2.35) at the surface, but at the inner radius I must satisfy eq. (2.17), considering only the linear Ohmic terms. This means that $\partial\beta/\partial r$ must vanish there, so

$$Cj_l(kr_{min}) + Dy_l(kr_{min}) + Ckr_{min}j_l'(kr_{min}) + Dkr_{min}y_l'(kr_{min}) = 0. \tag{2.38}$$

  Once again, I combine this equation with the zero boundary equation at the surface,

n	l	k_P	A/B	$k_{T,zbc}$	$(C/D)_{zbc}$	$k_{T,mbc}$	$(C/D)_{mbc}$
1	1	7.03266	1.07456	12.67071	-0.18517	6.51570	-0.40499
2	1	19.12793	3.49901	25.18557	-0.09278	18.92115	-0.12505
3	1	31.58468	5.86928	37.73441	-0.06187	31.45856	-0.07454
1	2	7.81795	10.93545	12.87682	1.65544	6.95730	0.50269
2	2	19.46616	-0.78889	25.29089	3.52035	19.06358	2.56764
3	2	31.79340	-0.43334	37.80492	5.33887	31.54365	4.41324
1	3	8.63565	-2.11402	13.17984	-1.82690	7.57117	1.76415
2	3	19.86013	0.43365	25.44808	-0.61489	19.27532	-0.90844
3	3	32.04098	1.14319	37.91043	-0.38745	31.67087	-0.47628

Table 2.1: First three radial modes for each of $l = 1, 2, 3$. The k_P are the values associated to the poloidal modes, while $k_{T,zbc}$ and $k_{T,scbc}$ are the values for the toroidal modes in the case of zero boundary conditions (for the subscript zbc) and Meissner boundary conditions (for the subscript mbc).

and obtain a transcendental equation and an equation for C/D,

$$y_l(kr_{min})j_l(k) - y_l(k)j_l(kr_{min}) + kr_{min}y_l'(kr_{min})j_l(k) - kr_{min}y_l(k)j_l'(kr_{min}) = 0$$
$$\frac{C}{D} = -\frac{y_l(k)}{j_l(k)}. \tag{2.39}$$

Solving equations (2.34), (2.37) and (2.39) for $l = 1, 2, 3$ and up to the third radial mode (for which I use the index $n = 1, 2, 3$), I obtain the values contained in Table 2.1. The most important thing to be noted from these values is that with zero boundary conditions the toroidal modes will decay much more rapidly than the corresponding poloidal modes, while with the Meissner boundary conditions the poloidal modes decay slightly faster than the toroidal ones.

2.3 Hall equilibria

Part of the purpose of this thesis is to test the stability of Hall equilibria, for which the Hall term is exactly equal to zero. If I take Eqs. (2.7) and equate the Hall term to zero,

then

$$\nabla\alpha \times \nabla\beta = 0 \tag{2.40}$$

$$\nabla[\chi\Delta^*\alpha] \times \nabla\alpha + \beta\nabla\chi \times \nabla\beta = 0. \tag{2.41}$$

The first of these equations is satisfied if and only if $\beta = \beta(\alpha)$, which can be used on the second equation to obtain that

$$\nabla[\chi\Delta^*\alpha + \chi\beta\beta'] \times \nabla\alpha = 0, \tag{2.42}$$

where $\beta' = \mathrm{d}\,\beta/\,\mathrm{d}\,\alpha$. This in turn means that the function inside the brackets must be a function of α, which I denote by $F(\alpha)$, so, after replacing $\chi = 1/(\varpi^2 n)$, I get that the functions α and β describe a Hall equilibrium field if and only if

$$\Delta^*\alpha + \beta\beta' = F(\alpha)nr^2\sin^2\theta, \tag{2.43}$$

for an arbitrary function $F(\alpha)$. In this work I will only analyse a single purely poloidal equilibrium field, which is the solution to this equation with the choice $F(\alpha) = F_0$ and $n = n_0$ constant. Looking for a separable solution of the form $\alpha = f(r)\sin^2\theta$ results in a simple differential equation for the function $f(r)$,

$$f'' - \frac{2}{r^2}f = F_0 n_0 r^2. \tag{2.44}$$

Lyutikov et al. (private communication) showed that a particular solution to this equation, subject to zero boundary condition for $\alpha(r_{min})$, a normalization such that the strength of the field at the poles is B_0 and a completely continuous magnetic field through the surface (conditions which in turn fix the value of F_0) is given in dimensionless form by the function

$$f(r) = \frac{(3r_{min}^5 - 5r_{min}^3)/r + 5r^2 - 3r^4}{4 - 10r_{min}^3 + 6r_{min}^5}, \tag{2.45}$$

so the equilibrium field I study is

$$\alpha = \frac{(3r_{min}^5 - 5r_{min}^3)/r + 5r^2 - 3r^4}{4 - 10r_{min}^3 + 6r_{min}^5}\sin^2\theta. \tag{2.46}$$

Chapter 3

Numerical methods

For the purpose of studying the evolution of an axially symmetric field in a neutron star crust, I have developed a FTCS (forward time centered space) code to solve the set of differential equations (2.11), where the temporal discretization is done via the forward Euler method, which is first order in time, while spatial derivatives are solved with a central difference scheme that is second order in space. This code is freely available for download at `https://gitorious.org/hall_evolution/hall_evolution`.

As is shown in Figure 3.1, the functions α and β are discretized in a regular spherical grid with N_θ points in the θ direction (including the axis) and N_r points in the radial direction (including the surface and the inner boundary) plus a point just outside the surface and one just below the inner boundary. These two additional points are required to set boundary conditions on the derivatives.

To describe the discretized values of the functions, I use the notation $\alpha^k_{i,j}$, where i and j denote the grid points as shown in Figure 3.1, and k denotes the timestep. The numerical method used for the temporal discretization of both equations is simply of the form

$$\alpha^{k+1}_{i,j} = \alpha^k_{i,j} + \Delta t \left(\frac{\partial \alpha}{\partial t}\right)^k_{i,j}. \tag{3.1}$$

However, the calculation of the time derivatives is done in fundamentally different ways for each of these functions. For the time derivative of α, I simply use the usual three-point

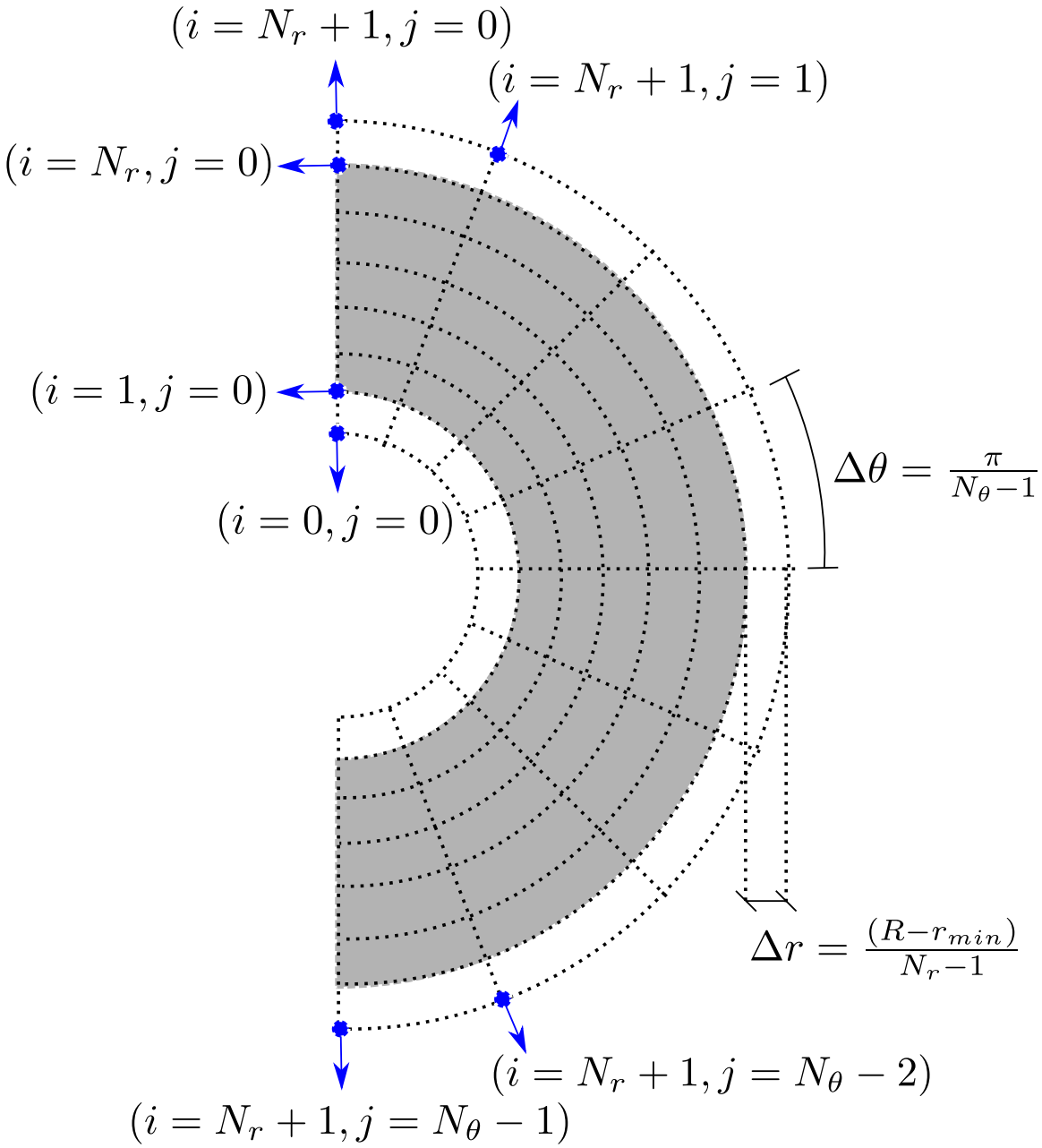

Figure 3.1: Spherical grid used to spatially discretize α and β.

stencil approximation to all the derivatives involved,

$$\left(\frac{\partial\alpha}{\partial t}\right)^k_{i,j} = \frac{\sin\theta_j \chi_{i,j}}{4\Delta r\Delta\theta}\Big[(\beta^k_{i,j+1}-\beta^k_{i,j-1})(\alpha^k_{i+1,j}-\alpha^k_{i-1,j}) - (\beta^k_{i+1,j}-\beta^k_{i-1,j})(\alpha^k_{i,j+1}-\alpha^k_{i,j-1})\Big] + R_B^{-1}\eta_{i,j}\,(\Delta^*\alpha)^k_{i,j}\,, \tag{3.2}$$

where $\theta_j = j\Delta\theta$ and $(\Delta^*\alpha)^k_{i,j}$ is solved as

$$(\Delta^*\alpha)^k_{i,j} = \frac{\alpha^k_{i+1,j}+\alpha^k_{i-1,j}-2\alpha^k_{i,j}}{(\Delta r)^2} + \frac{\alpha^k_{i,j+1}+\alpha^k_{i,j-1}-2\alpha^k_{i,j}}{(r_j)^2\,(\Delta\theta)^2} - \cot\theta_j\frac{\alpha^k_{i,j+1}-\alpha^k_{i,j-1}}{2(r_j)^2\Delta\theta}, \tag{3.3}$$

where $r_j = (i-1)\Delta r + r_{min}$. For the time derivative of β, I take advantage of the flux-conservative properties of the equation, by using the discretization

$$\begin{aligned}\frac{1}{\sin\theta_j}\left(\frac{\partial\beta}{\partial t}\right)^k_{i,j} = \frac{1}{\Delta r}\Bigg(&\left[\chi\Delta^*\alpha\frac{\partial\alpha}{\partial\theta}+\chi\beta\frac{\partial\beta}{\partial\theta}+R_B^{-1}\frac{\eta}{\sin\theta}\frac{\partial\beta}{\partial r}\right]^k_{i+1/2,j} \\ &-\left[\chi\Delta^*\alpha\frac{\partial\alpha}{\partial\theta}+\chi\beta\frac{\partial\beta}{\partial\theta}+R_B^{-1}\frac{\eta}{\sin\theta}\frac{\partial\beta}{\partial r}\right]^k_{i-1/2,j}\Bigg) \\ +\frac{1}{\Delta\theta}\Bigg(&\left[-\chi\Delta^*\alpha\frac{\partial\alpha}{\partial r}-\chi\beta\frac{\partial\beta}{\partial r}+R_B^{-1}\frac{\eta}{r^2\sin\theta}\frac{\partial\beta}{\partial\theta}\right]^k_{i,j+1/2} \\ &-\left[-\chi\Delta^*\alpha\frac{\partial\alpha}{\partial r}-\chi\beta\frac{\partial\beta}{\partial r}+R_B^{-1}\frac{\eta}{r^2\sin\theta}\frac{\partial\beta}{\partial\theta}\right]^k_{i,j-1/2}\Bigg),\end{aligned} \tag{3.4}$$

where $(i\pm1/2, j)$ and $(i, j\pm1/2)$ denote edge-centered values of the grid, solved for example

as

$$\left[\chi\Delta^*\alpha\frac{\partial\alpha}{\partial\theta}+\chi\beta\frac{\partial\beta}{\partial\theta}+R_B^{-1}\frac{\eta}{\sin\theta}\frac{\partial\beta}{\partial r}\right]^k_{i+1/2,j}= \\ \chi_{i+1/2,j}\frac{[\Delta^*\alpha]^k_{i+1,j}+[\Delta^*\alpha]^k_{i,j}}{2}\frac{[\partial\alpha/\partial\theta]^k_{i+1,j}+[\partial\alpha/\partial\theta]^k_{i,j}}{2} \\ \chi_{i+1/2,j}\frac{[\beta]^k_{i+1,j}+[\beta]^k_{i,j}}{2}\frac{[\partial\beta/\partial\theta]^k_{i+1,j}+[\partial\beta/\partial\theta]^k_{i,j}}{2} \\ +\frac{R_B^{-1}\eta_{i+1/2,j}}{2\sin\theta_j}\left(\frac{\beta^k_{i+1,j}-\beta^k_{i,j}}{\Delta r}\right), \tag{3.5}$$

from which the mesh-centered values are solved using the regular three-point approximation for the derivatives of α and β together with eq. (3.3) for $\Delta^*\alpha$, and the remaining edge-centered values can be solved exactly. The main feature of the discretization given by eq. (3.4) is that the time derivative of the quantity

$$F=\sum_{i=1}^{N_r}\sum_{j=1}^{N_\theta-1}\frac{\beta^k_{i,j}}{\sin\theta_j} \tag{3.6}$$

will depend only on boundary values of the functions and its derivatives. This embodies the-flux conservation property of the equation for β.

For the evolution of β, I use eq. (3.4) for the grid points with $2\leq i\leq N_r-1$ and $1\leq j\leq N_\theta-1$. For the case of α, eq. (3.2) is used to solve the evolution for the grid points with $2\leq i\leq N_r$ and $1\leq j\leq N_\theta-1$. All other points on the grid are evolved using information from the boundary conditions.

3.1 Boundary conditions

In this section, I describe how the boundary conditions described in §2.1 are implemented in this finite difference-scheme. The zero boundary conditions are trivial, but the condition for α at the surface and the Meissner boundary conditions must be treated with care.

For the surface of the star, I have the boundary condition given by eq. (2.24), which

can be expressed in finite difference (and dimensionless form) as

$$\frac{\alpha^k_{N_r+1,j} - \alpha^k_{N_r-1,j}}{2\Delta r} = -\sum_{l=1}^{L} l a_l \sqrt{\frac{2l+1}{4\pi}} \sin\theta_j P_l^1(\cos\theta_j). \tag{3.7}$$

This expression gives the value of $\alpha^k_{N_r+1,j}$ at each timestep. The sum must be limited to a finite number of multipoles L, and the a_l are given by eq. (2.22), but with the integral solved using the trapezoidal rule,

$$a_l = \frac{l}{l+1}\sqrt{\pi(2l+1)} \sum_{j=0}^{N_\theta - 1} \frac{(\alpha^k_{N_r,j} + \alpha^k_{N_r,j+1})}{2} P_l^1(\cos\theta_{j+1/2})\Delta\theta. \tag{3.8}$$

To evolve the function α right at the surface it is necessary to evaluate the radial derivative of β. For this purpose, I set $\beta^k_{r_{min}+1,j}$ in such a way that the derivative at the surface is the same as solving the derivative backwards, i.e.

$$\frac{\beta^k_{r_{min}+1,j} - \beta^k_{r_{min}-1,j}}{2\Delta r} = \frac{\beta^k_{r_{min},j} - \beta^k_{r_{min}-1,j}}{\Delta r}. \tag{3.9}$$

To implement the Meissner boundary conditions given by eqs. (2.17), I solve for $\alpha^k_{0,j}$ and $\beta^k_{0,j}$ from the discretized versions of these,

$$\begin{aligned} 0 =& \chi_{1,j}\beta^k_{1,j}\frac{\beta^k_{1,j+1} - \beta^k_{1,j-1}}{2\Delta\theta} + R_B^{-1}\frac{\eta_{1,j}}{\sin\theta_j}\frac{\beta^k_{2,j} - \beta^k_{0,j}}{2\Delta r} \\ 0 =& \sin\theta_j \chi_{1,j}\frac{\beta^k_{1,j+1} - \beta^k_{1,j-1}}{2\Delta\theta}\frac{\alpha^k_{2,j} - \alpha^k_{0,j}}{2\Delta r} + R_B^{-1}\eta_{1,j}\frac{\alpha^k_{2,j} + \alpha^k_{0,j}}{(\Delta r)^2}, \end{aligned} \tag{3.10}$$

from which I get

$$\begin{aligned} \beta^k_{0,j} =& \beta^k_{2,j} + \frac{R_B}{n_{i,j}\eta_{i,j} r^2_{min}\sin\theta_j}\frac{\Delta r}{\Delta\theta}\left(\beta^k_{1,j+1} - \beta^k_{1,j-1}\right) \\ \alpha^k_{0,j} =& \alpha^k_{2,j}\frac{(\beta^k_{1,j+1} - \beta^k_{1,j-1})\Delta r + 4n_{i,j}\eta_{i,j}R_B^{-1}r^2_{min}\sin\theta_j\Delta\theta}{(\beta^k_{1,j+1} - \beta^k_{1,j-1})\Delta r - 4n_{i,j}\eta_{i,j}R_B^{-1}r^2_{min}\sin\theta_j\Delta\theta}. \end{aligned} \tag{3.11}$$

Unfortunately, the denominator in this last expression can get very close to zero, causing numerical problems for simulations with large R_B. Better stability can be achieved with

grids that have $N_r > N_\theta$, for which the grid will much more defined in the radial direction than the angular one.

The only thing remaining is a way to time-evolve $\beta^k_{1,j}$ for the Meissner boundary conditions. To do this, I use a modified form of eq. (3.4),

$$\begin{aligned}\frac{1}{\sin\theta_j}\left(\frac{\partial\beta}{\partial t}\right)^k_{1,j} = \frac{1}{\Delta r/2}\Bigg(&\left[\chi\Delta^*\alpha\frac{\partial\alpha}{\partial\theta}+\chi\beta\frac{\partial\beta}{\partial\theta}+R_B^{-1}\frac{\eta}{\sin\theta}\frac{\partial\beta}{\partial r}\right]^k_{1+1/2,j}\\ &-\left[\chi\Delta^*\alpha\frac{\partial\alpha}{\partial\theta}+\chi\beta\frac{\partial\beta}{\partial\theta}+R_B^{-1}\frac{\eta}{\sin\theta}\frac{\partial\beta}{\partial r}\right]^k_{1,j}\Bigg)\\ +\frac{1}{\Delta\theta}\Bigg(&\left[-\chi\Delta^*\alpha\frac{\partial\alpha}{\partial r}-\chi\beta\frac{\partial\beta}{\partial r}+R_B^{-1}\frac{\eta}{r^2\sin\theta}\frac{\partial\beta}{\partial\theta}\right]^k_{1,j+1/2}\\ &-\left[-\chi\Delta^*\alpha\frac{\partial\alpha}{\partial r}-\chi\beta\frac{\partial\beta}{\partial r}+R_B^{-1}\frac{\eta}{r^2\sin\theta}\frac{\partial\beta}{\partial\theta}\right]^k_{1,j-1/2}\Bigg).\end{aligned} \tag{3.12}$$

Noting that $\alpha^k_{1,j} = 0$ together with the first of the Meissner boundary conditions (2.24) implies that the first of the terms in the previous equations is equal to zero, I have that

$$\begin{aligned}\frac{1}{\sin\theta_j}\left(\frac{\partial\beta}{\partial t}\right)^k_{1,j} = \frac{1}{\Delta r/2}&\left[\chi\Delta^*\alpha\frac{\partial\alpha}{\partial\theta}+\chi\beta\frac{\partial\beta}{\partial\theta}+R_B^{-1}\frac{\eta}{\sin\theta}\frac{\partial\beta}{\partial r}\right]^k_{1+1/2,j}\\ +\frac{1}{\Delta\theta}\Bigg(&\left[-\chi\Delta^*\alpha\frac{\partial\alpha}{\partial r}-\chi\beta\frac{\partial\beta}{\partial r}+R_B^{-1}\frac{\eta}{r^2\sin\theta}\frac{\partial\beta}{\partial\theta}\right]^k_{1,j+1/2}\\ &-\left[-\chi\Delta^*\alpha\frac{\partial\alpha}{\partial r}-\chi\beta\frac{\partial\beta}{\partial r}+R_B^{-1}\frac{\eta}{r^2\sin\theta}\frac{\partial\beta}{\partial\theta}\right]^k_{1,j-1/2}\Bigg).\end{aligned} \tag{3.13}$$

3.2 Variable time step

Usually it will be the case that some time intervals in the simulation will require a much smaller Δt to converge without producing numerical instabilities. Since Hall drift will advect field lines with the electron velocity $\boldsymbol{v}_e = -\boldsymbol{j}/(ne)$, I have a Courant condition of the form

$$\frac{|\boldsymbol{v}_e|\Delta t}{\Delta l} < k_c, \tag{3.14}$$

where $k_c < 1$ is chosen at the beginning of each simulation and Δl is the smaller dimension of a grid cell. Using that $\boldsymbol{j} = c(\nabla \times \boldsymbol{B})/(4\pi)$, the timestep is solved as

$$\Delta t = k_c \left(\frac{4\pi n e}{c} \right) \frac{\Delta l}{|\nabla \times \boldsymbol{B}|}, \tag{3.15}$$

which is exactly the same condition used by Viganò et al. (2012). Considering that in the thin crust, unless N_θ is much larger than N_r, the smallest dimension of a grid cell will always be Δr, the critical timestep in dimensionless form is

$$\Delta t = k_c \frac{n \Delta r}{|\nabla \times \boldsymbol{B}|}. \tag{3.16}$$

At each step of the simulation, this is evaluated at all points in the grid, and the smallest value is chosen. In order to avoid having the timestep increase indefinitely as Ohmic diffusion becomes dominant, I also define a dissipative timestep,

$$\Delta t = k_c \frac{(\Delta r)^2}{\eta}, \tag{3.17}$$

and the smallest of the two values is used at each step of the simulation.

Although in principle I need $k_c < 1$, in the simulations performed for this thesis numerical problems arose when k_c was chosen close to unity, sometimes requiring values as small as $k_c = 0.01$ for the simulations to converge. The need for such small timesteps might be related to the use of purely explicit (and first order in time) methods for the time evolution.

3.3 Test cases

Now I consider two tests applied to the code to see if it describes the evolution correctly: (1) comparison of simulations with pure Ohmic decay with the analytical solutions, (2) evolution of purely toroidal fields and comparison with the results of Urpin and Shalybkov (1991), and (3) a comparison with the spectral code used by Hollerbach and Rüdiger (2002, 2004).

3.3.1 Ohmic modes

Testing the evolution through pure Ohmic dissipation is straightforward, because I know exact analytical solutions, which is not the case of combined Hall+Ohm simulations. This is a two-step process: it must be verified that the decay rates are solved correctly, and that the evolution of an Ohm mode preserves its structure. I describe here this analysis only for the fundamental mode for the case of constant resistivity, but this was done also for higher order modes with successful results.

In order to verify that the structure of Ohm modes is preserved, I perform simulations using the fundamental toroidal and poloidal Ohm modes as initial conditions, and after $0.1t_{Ohm}$, I evaluate in every point of the grid[1]

$$A_{i,j} = 1 - \frac{\alpha_{i,j}^{final}}{\alpha_{i,j}^{initial} e^{-0.1k_{11p}^2}}, \qquad B_{i,j} = 1 - \frac{\beta_{i,j}^{final}}{\beta_{i,j}^{initial} e^{-0.1k_{11t}^2}}, \tag{3.18}$$

where k_{11p} and k_{11t} are the values listed in §2.2 for the fundamental poloidal and toroidal Ohm modes respectively, and the final and initial superscripts indicate the values at the end and the beginning of the simulation. These values should all be very close to zero, with a general digression from that value due to the difference in the numerical and analytical decay rates, and a slight difference from point to point due to the difference in structure between the numerical and analytical modes. As the resolution is improved, these values should all approach zero. The timestep used is given by the critical timestep for Ohmic diffusion described in §3.2, with $k_c = 0.1$. Figs. 3.2 and 3.3 show $A_{i,j}$ and $B_{i,j}$ respectively plotted for different resolutions and zero boundary conditions, and it is seen that as resolution improves, agreement between the structure of the numerical and analytical Ohm modes improves. However, the toroidal field shows an important error on the lowest resolution case, but this is just due to a large timestep which artificially produces much stronger dissipation (this is not observed in the poloidal field, probably because its decay timescale is much larger).

For the case of the poloidal modes, however, there is a systematic disagreement near the poles that is closely related to errors in the coefficients of the multipolar expansion. For the fundamental mode, which is a pure dipole, all multipole coefficients except for a_1

[1] The time $0.1t_{Ohm}$ is enough to visualize the full impact of Ohmic dissipation, as, for instance, the decay timescale of the fundamental poloidal Ohm mode is $\sim 0.02t_{Ohm}$

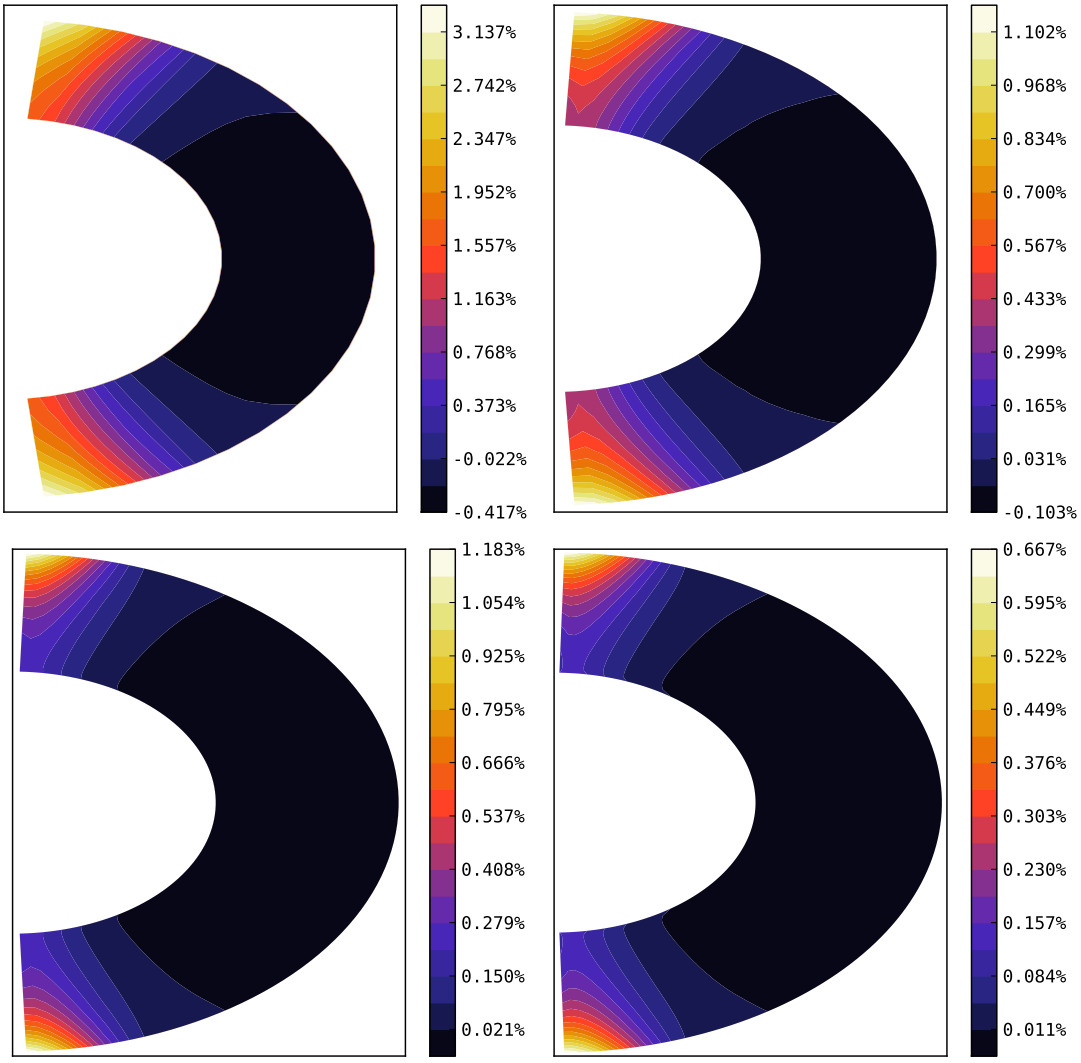

Figure 3.2: Plots of $A_{i,j}$ as described in Eq. (3.18) for different resolutions. From left to right and top to bottom, the resolutions used are $10 \times 30 \times 6$, $20 \times 60 \times 12$, $30 \times 90 \times 18$ and $40 \times 120 \times 24$, where the numbers represent N_r, N_θ and the maximun multipole L used in the multipole expansion. It can be seen that the values approach unity as the resolution is improved. The errors in the poles are due to errors in the calculated multipole coefficients. The width of the crust is doubled to aid visualization.

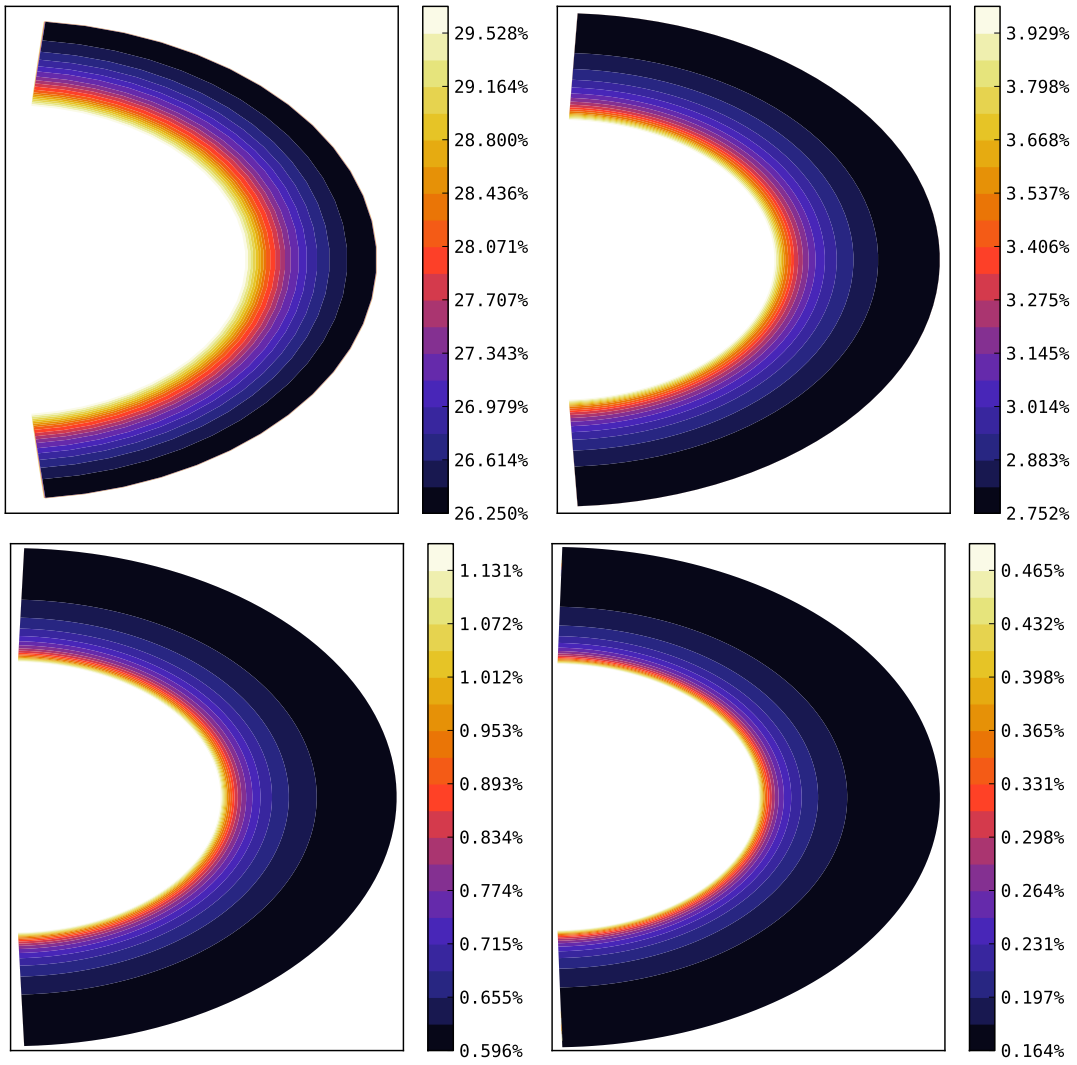

Figure 3.3: Plots of $B_{i,j}$ as described in Eq. (3.18) for different resolutions in the case of zero boundary conditions. From left to right and top to bottom, the resolutions used are 10×30, 20×60, 30×90 and 40×120, where the numbers represent N_r and N_θ. It can be seen that the values approach unity as the resolution is improved. However, very low resolution grids produce a significant error in the numerical solution, that can be fixed by reducing the timestep. The width of the crust is doubled to aid visualization.

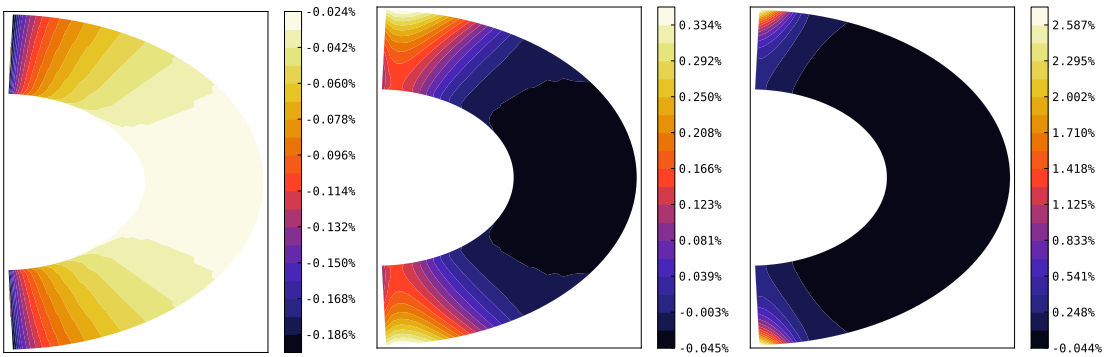

Figure 3.4: Plots of $A_{i,j}$ as described in Eq. (3.18) with $N_r = 30$ and $N_\theta = 90$, but with different numbers of multipoles used. From left to right, the maximun multipole used is $L = 1, 9, 27$. As more multipoles are used, the systematic error to the pole increases. The width of the crust is doubled to aid visualization.

should be equal to zero, however errors from the numerical integrations produce nonzero values on higher order multipoles which are responsible for this systematic error. Fig. 3.4 shows how $A_{i,j}$ changes by using a different number of multipoles. As can be seen, the number of multipoles used must be significantly smaller than N_θ, otherwise, an important disagreement between the analytical and numerical solutions occurs. So, in order to be on the safe side, in all simulations made for this thesis the maximum number of multipoles used does not exceed $L = 0.2N_\theta$.

The same analysis was repeated for the toroidal field in the case of Meissner boundary conditions, and the results were very similar to the ones of Fig. 3.3, except the lowest resolution had a better agreement, probably because the decay timescale with Meissner boundary conditions is much larger.

So, the structure of the modes is well resolved by my simulations, and what is left is to check the numerical values obtained for the k_{11p} and k_{11t}. This is done by fitting the decay of the poloidal and magnetic energies, and the results of doing this are contained in Table 3.1, where it is seen that the numerical values approach the analytical ones as resolution is improved. These values are probably more dependant on the size of the timestep than the spatial resolution, but I did not check explicitly for that.

Resolution ($N_r \times N_\theta \times L$)	τ_{11p}	τ_{11t} without Meissner	τ_{11t} with Meissner
$10 \times 30 \times 6$	0.0202314	0.0061070	0.0235731
$20 \times 60 \times 12$	0.0202220	0.0062171	0.0235589
$30 \times 90 \times 18$	0.0202204	0.0062261	0.0235565
$40 \times 120 \times 24$	0.0202198	0.0062279	0.0235557
Analytical	0.0202191	0.0062287	0.0235547

Table 3.1: Numerical values for the decay timescales of the fundamental poloidal and toroidal modes (τ_{11p} and τ_{11t} respectively) measured in terms of τ_{Ohm} for different resolutions, compared to the known analytical values. Errors on the numerical values are not shown, since they are much smaller than the number of significant digits shown. The timesteps used for each of the resolutions are 7.72×10^{-5}, 1.73×10^{-5}, 7.43×10^{-6} and 4.11×10^{-6} in units of t_{Ohm}.

3.3.2 Purely toroidal fields

As said in §2, purely toroidal fields remain toroidal under Hall drift. Urpin and Shalybkov (1991) already studied this case, considering a star with constant electron density and resistivity that through its entire radius evolves via Hall drift and Ohmic diffusion. They showed that the field drifted towards the surface, where it forms a very strong current sheet with the consequence of rapid Ohmic dissipation. As R_B increases, this current sheet becomes stronger, producing faster dissipation (however, this is not the case if the electron density decreases towards the surface (Reisenegger et al. 2007)). These results are shown in Fig. 3.5.

An older version of the code developed could deal with purely toroidal fields when $r_{min} = 0$, but the current one is not designed to cope with that. Even though a direct comparison was made with the work of Urpin and Shalybkov (1991) using the older code, here I present results using the current version, with the field restricted to a crust of size $0.25R$. I care most about the qualitative behaviour rather than the detailed quantitative evolution, so this will suffice. Fig. 3.6 shows the evolution of the fundamental toroidal Ohm mode, where it is shown that the field drifts to the surface producing a strong current sheet, where it undergoes rapid dissipation until the evolution becomes dominated by Ohmic diffusion. From that point forward, the field starts settling back to the fundamental Ohm mode.

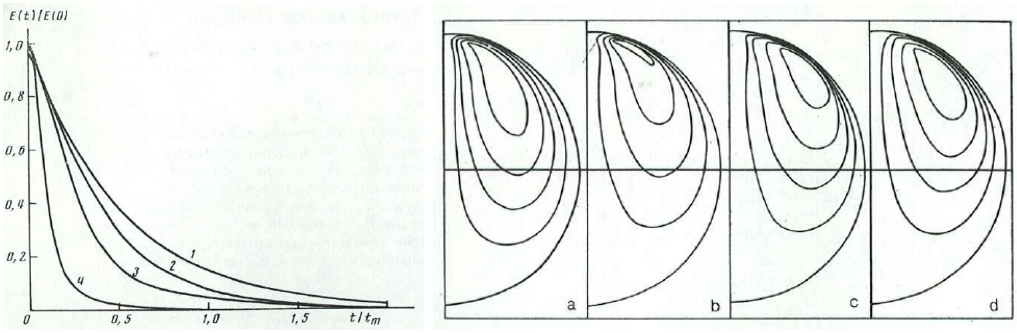

Figure 3.5: Evolution of the fundamental toroidal Ohm mode in a homogeneous star with no core (i.e. $r_{min} = 0$). The plot on the left shows the decay of magnetic energy as a function of time measured in units of the decay timescale of the fundamental toroidal Ohm mode for $R_B = 0, 25, 50, 200$. On the right contours of the toroidal magnetic field are shown for different snapshots of a simulation with $R_B = 25$, showing the field drifting to the surface. Figures taken from Urpin and Shalybkov (1991).

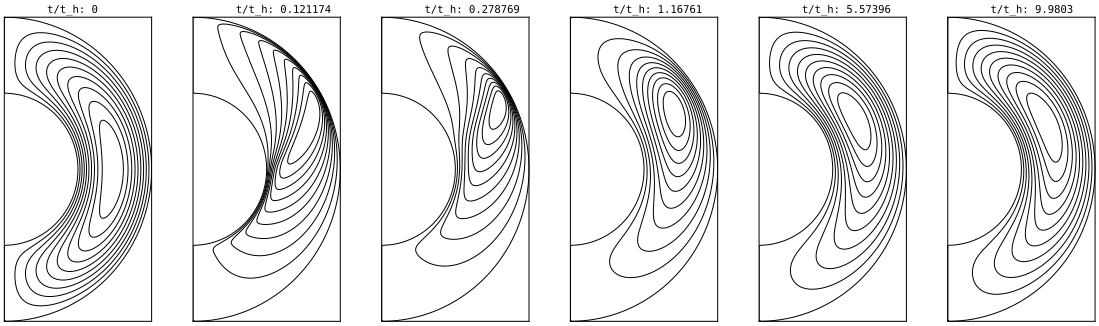

Figure 3.6: Contours of toroidal magnetic field for the evolution of the fundamental toroidal Ohm mode in a model star with $r_{min} = 0.75$ and $R_B = 100$. The field drifts to the surface producing strong currents and dissipation. The width of the crust is doubled to aid visualization.

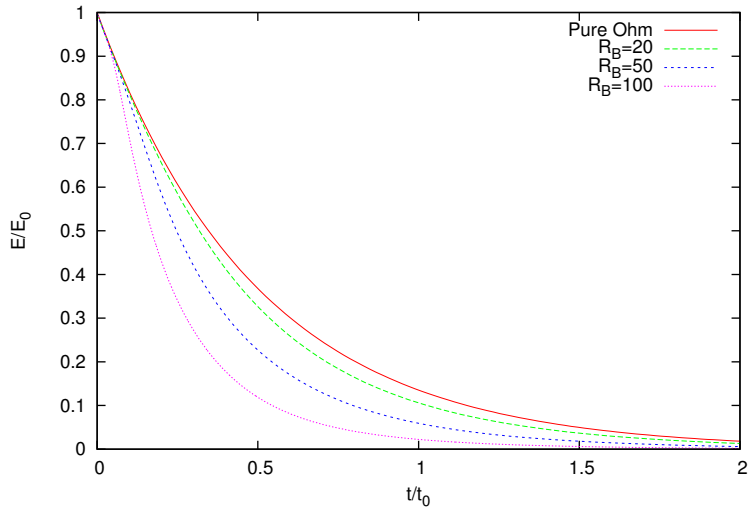

Figure 3.7: Evolution of the energy of the toroidal field as a function of time measured in units of the decay timescale of the fundamental toroidal Ohm mode.

3.3.3 Comparison with Hollerbach's spectral code

Through our collaborator Jaime Hoyos from the "Universidad de Medellín" in Colombia, I had access to the spectral code used in the simulations of Hollerbach and Rüdiger (2002, 2004). He ran 2 test cases in order to compare them with the code developed for this thesis. As Hollerbach's code only supports zero boundary conditions, the tests were restricted to these. The choice of initial conditions were combinations of the fundameental poloidal and toroidal Ohmic modes for zero boundary conditions described in §2.2 for $r_{min} = 0.75$, with the following choice of coefficients,

- Test 1: $A = -0.16764$ and $C = -2.00235$, which gives a predominantly toroidal field. (i.e. the energy of the toroidal component is significantly larger than the energy of the poloidal component)
- Test 2: $A = -0.55882$ and $C = -.60070$, which gives a predominantly poloidal field.

The resolution used when running these simulations with Hollerbach's spectral code was an expansion in terms of 25 radial and 25 latitudinal modes, so I ran the simulations with my code using 25 radial and 25 latitudinal grid points with $L = 5$ for the multipole

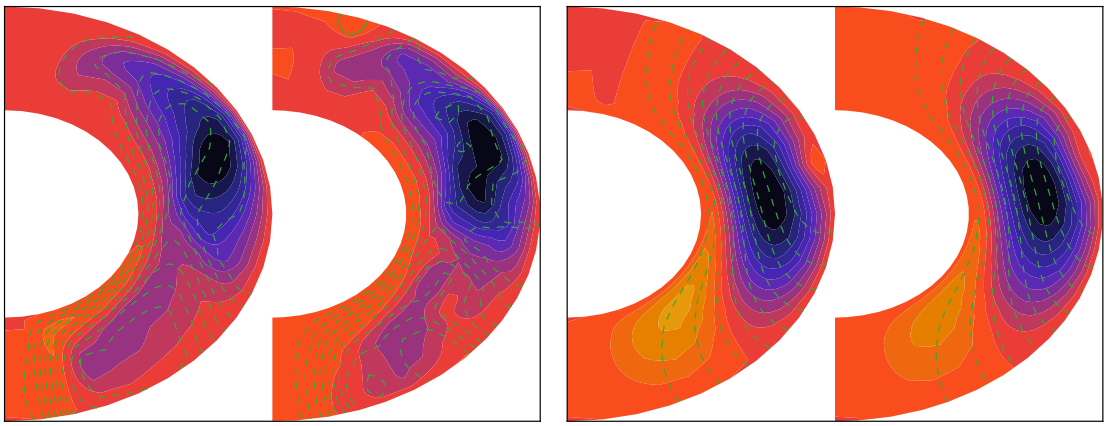

Figure 3.8: Snapshots at two different times in the evolution of both test cases of §3.3.3. The color plot shows the intensity of β, while the contours are lines of constant α The size of the crust is doubled to ease visualization. For both images, the plot on the left is done with the code developed for this thesis, while the one on the right is done with Hollerbach's spectral code. The plots on the left are for the first test case, at a time $t = 0.2t_{Hall}$ with Hollerbach's code, and $t = 0.194t_{Hall}$ with the code developed for this thesis. The plots on the right are for the second test case, at a time $t = 0.7t_{Hall}$ with Hollerbach's code, and $t = 0.701t_{Hall}$ with the code developed for this thesis. The difference in time is due to the adaptative timestep used in the simulations done with my code.

expansion outside the star. The simulations were ran using $R_B = 100$, and Figs. 3.8 and 3.9 show snapshots of the structure of the field and the evolution of the magnetic energy respectively. It can be seen that even at this very low resolution both the structure and the energetics are very consistent for simulations done with each of the codes. Differences can be seen on the structure of the field obtained, but these are most likely due to the mismatch between simulation times compared (due to the adaptative code not allowing a precise simulation time to be logged), and that Hollerbach's code outputs values of β and α in points which are not evenly spaced in the latitudinal direction, which at this low resolution can produce notorious differences in the visualization. Also, the evolution of the energies of the poloidal and toroidal components shows some differences, which are larger for the first test case. This differences can be attributed in part to a slight difference in the result of computing the energies with one code or the other, as can be seen from the initial energies not matching precisely. The larger mismatch on the first case is expected, as the

evolution in this case produces structure smaller scales which cannot be properly resolved with the low resolution used, and in fact, performing simulations with my code and higher resolutions gave slightly different results for this case, though keeping the overall behavior, which indicates that at this low resolution the results have not converged yet.

Since the implementation of the Hollerbach's spectral code is significantly different from ours, and it also includes an additional criteria over the evolution of the energy to check for the validity of its results, the very positive outcome of this comparison is indicative that the implementation is correct, at least for the case of zero boundary conditions.

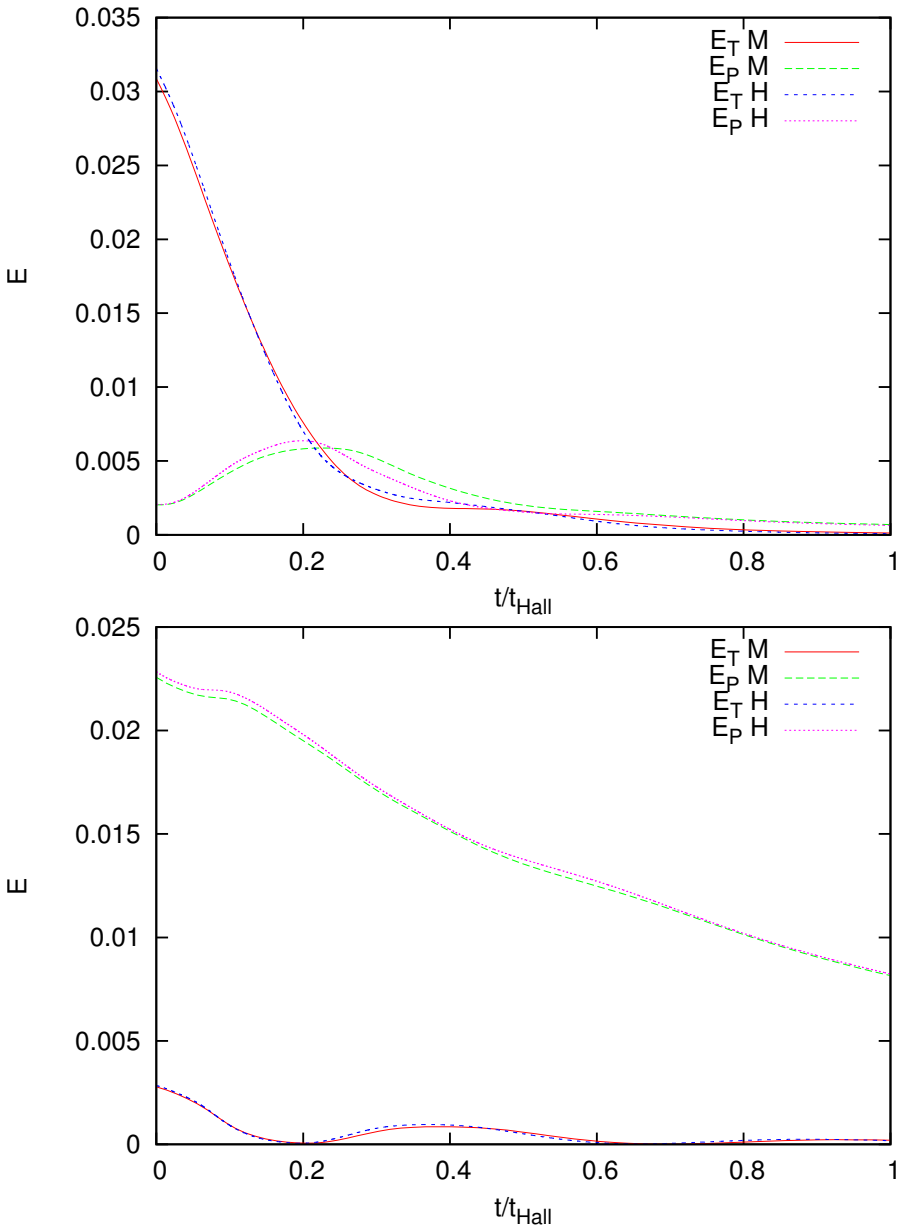

Figure 3.9: Evolution of the toroidal and (internal) poloidal energies for both test cases of §3.3.3 as a function of t/t_{Hall}. "M" (standing for Marchant) refers to simulations done with the code developed for this thesis, while "H" refers to the code used by Hollerbach and Rüdiger (2002, 2004).

Chapter 4

Results and analysis

4.1 Fields with dominant poloidal or toroidal components

During the testing of the code, it became apparent that in models with constant electron density and resistivity the evolution was significantly different depending on whether the poloidal or the toroidal component is dominant, a fact that was independently discovered and published by Kojima and Kisaka (2012). However, their analysis is not very detailed, and it is not very clear how they normalize their fields in order to compare each case. As the value of R_B is fundamentally dependent on the meaning I give to the characteristic field B_0, it is desirable to choose this value in a physically unambiguous way. For the purpose of this section, I will consider combinations of the fundamental poloidal and fundamental toroidal Ohmic modes, chosen in such a way that the total magnetic energy (including the energy of the field outside the star) satisfies

$$E = \frac{B_0^2}{8\pi} V_{crust}, \tag{4.1}$$

where V_{crust} is the volume of the crust. Defining $\boldsymbol{B}_{11p}$ and $\boldsymbol{B}_{11t}$, the fundamental poloidal and toroidal modes, in such a way that each of these satisfy the previous equation, I study combinations of the form

$$\boldsymbol{B} = \sqrt{(E_P/E)}\boldsymbol{B}_{11p} + \sqrt{(1 - E_P/E)}\boldsymbol{B}_{11t}, \tag{4.2}$$

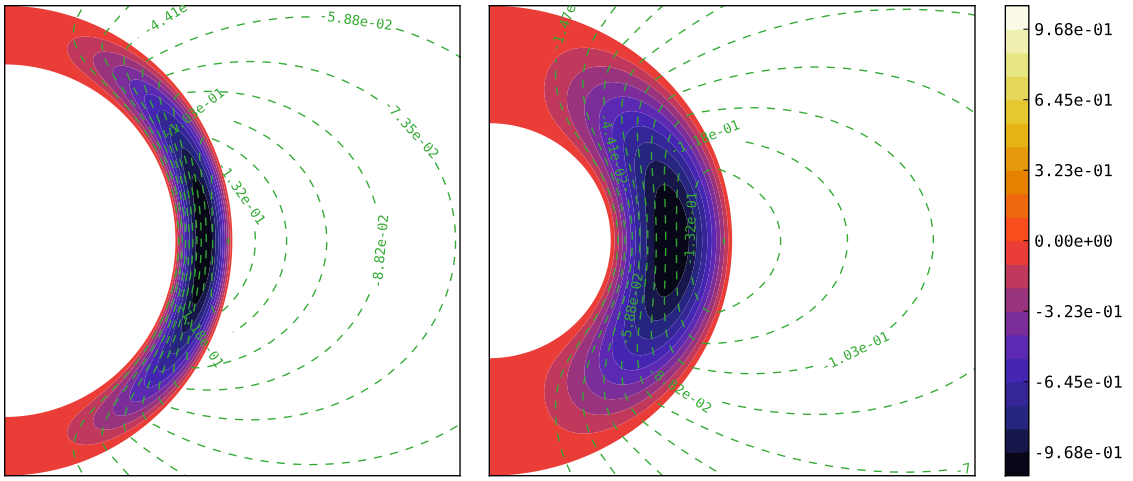

Figure 4.1: Expansion of the crust for visualization purposes. The plot on the left shows the field given by Eq. (4.2) with $E_P/E = 0.5$, and the crust and outer region in their correct sizes. The color plot is for the toroidal field function β, while the contours are for the poloidal field function α. On the left the same field is plotted, but with the crust size and the radial distance from the surface size doubled so field lines do not appear discontinuous.

all of which have the same total energy, and for which the relevance of each component is given by the ratio of poloidal to total energy E_P/E. For most of the analysis I will use zero boundary conditions, and compare in the end for some cases how the results are modified by the inclusion of Meissner boundary conditions. This is mainly because the Meissner boundary conditions as implemented here are prone to numerical problems, and cases of high R_B are computationally expensive to study. In the normalization used here, the maximum value of $\boldsymbol{B}_{11t}$ is of the order of $1.75B_0$, which can be compared for instance with the normalization used by Hollerbach and Rüdiger (2002), who choose $B_{max} = B_0$. The practical meaning of this is that my simulations with predominantly toroidal fields done with $R_B = 100$ should be comparable to their simulations with $R_B = 200$.

In order to visualize the results of the simulations, I will plot the values of β as a color scale together with contour lines of α, which represent field lines. The size of the crust chosen for the simulations is $R - r_{min} = 0.25R$, and in the plots the width of the crust will be shown expanded to $0.5R$, together with an appropriate rescaling outside the star

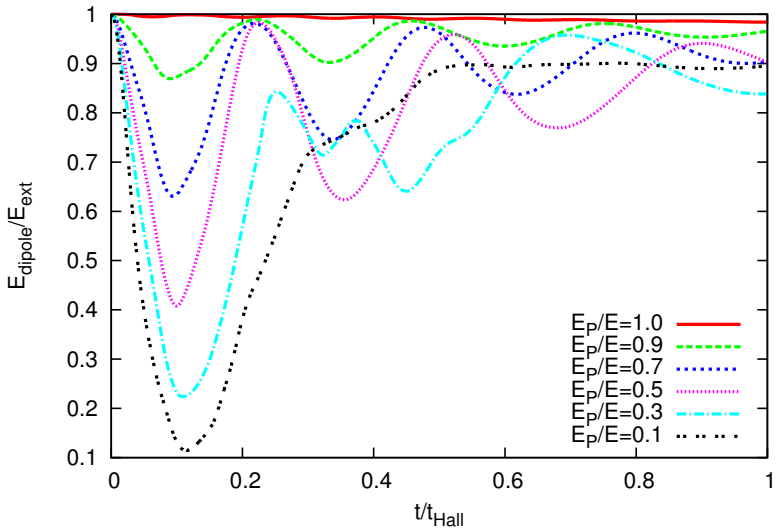

Figure 4.2: Fraction of the external energy contained in a dipole for different initial values of E_P/E. As the toroidal field becomes more important, energy is transferred to higher multipoles at the beginning of the evolution. Fields with a larger toroidal component rapidly decay, thus increasing the effective Hall timescale, so oscilatory phenomena after the first peak in multipole energy happens much slower than for poloidally dominated fields.

in order for poloidal field lines not to look discontinuous. This deformation is explicitly shown in Fig. 4.1.

In order to properly explore how the poloidally dominated regime is separated from the toroidally dominated one, I perform simulations using the field of Eq. (4.2) with $E_P = 1, 0.9, 0.7, 0.5, 0.3$ and $0, 1$. For all these simulations I use a resolution of 30 radial and 150 angular steps, and a factor of the critical timestep that varies between $k_c = 0.01$ and $k_c = 0.025$ (for higher values of k_c the simulations present numerical issues). As an example, Figs. 4.3 and 4.4 show the simulations with $E_P/E = 0.9$ and $E_P/E = 0.1$ respectively. As can be seen from this plots, the poloidally dominated field evolves with what appears to be stable oscillations, without much digression from the original dipole field, but the toroidally dominated field concentrates field lines much closer to one of the poles, which transfers a lot of energy to higher order multipoles, as shown in Fig. 4.2.

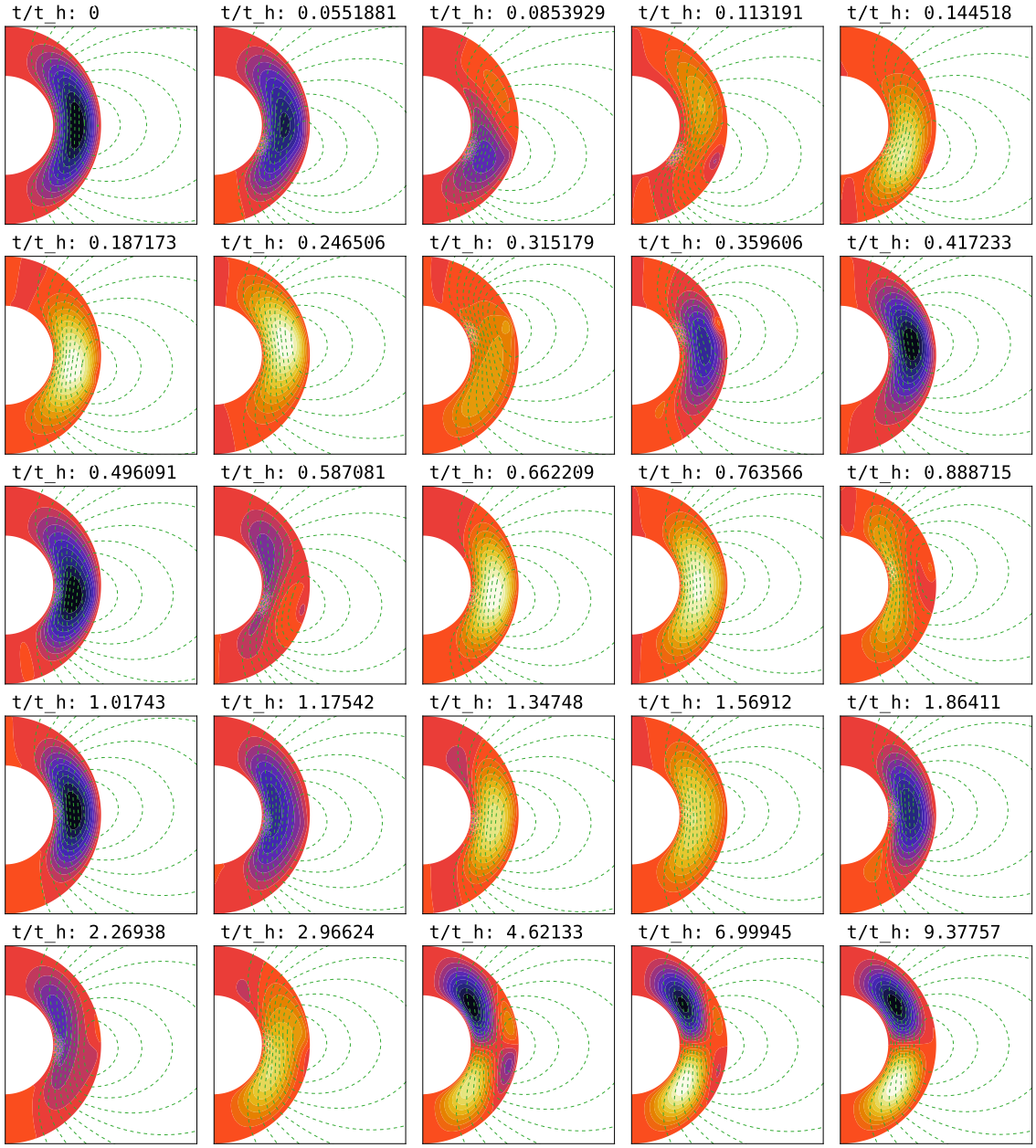

Figure 4.3: Evolution of a poloidally dominated field given by Eq. (4.2) with $E_P/E = 0.9$. The current associated to the toroidal field drags poloidal field lines to one of the poles, after which the bending of poloidal field lines completely changes the direction of the toroidal field. The poloidal field lines are then dragged to the opposite pole, where the process is repeated until the evolution is dominated by Ohmic dissipation with a mixture of the fundamental poloidal Ohm mode and the $n = 1, l = 2$ toroidal Ohm mode.

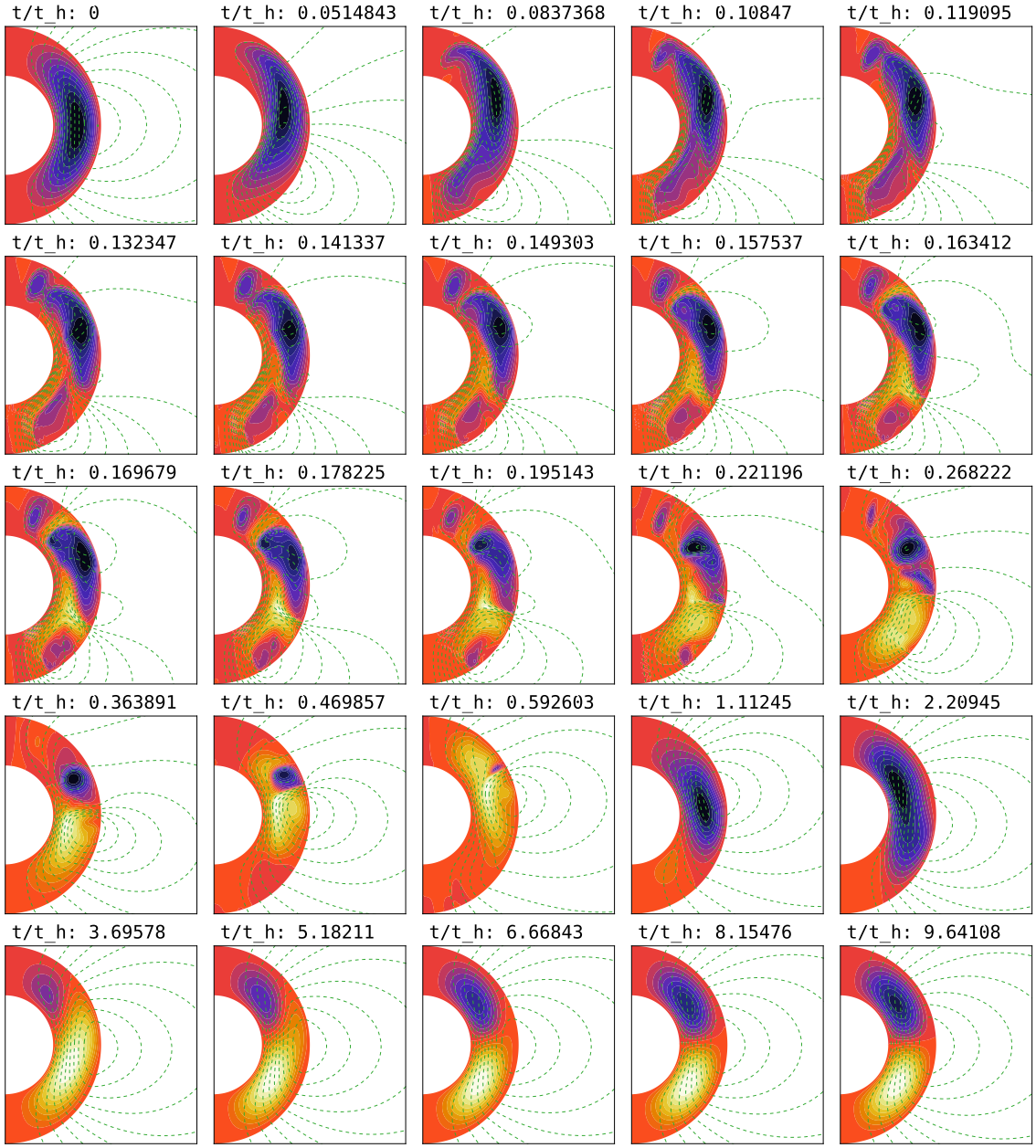

Figure 4.4: Evolution of a toroidally dominated field given by Eq. (4.2) with $E_P/E = 0.1$. The currents associated to the toroidal field drag poloidal field lines to one of the poles, just as was the case with the poloidally dominated field. The toroidal field produces structure on smaller scales that rapidly dissipates while it also feeds energy to the poloidal field. which eventually becomes dominant, behaving in what follows just as described before for an initially dominant poloidal field.

Another major feature that is readily visible is that the toroidal field forms much smaller structures with stronger currents associated. This produces very strong field dissipation, that drives the field to equipartition, and from that point forward, the poloidal field becomes progressively more dominant. After reaching the poloidally dominant configuration, the field evolves through regular oscillations. Eventually, Hall drift becomes irrelevant due to the dissipation of the field, and Ohmic decay turns the field into a combination of the fundamental poloidal Ohm mode, together with the $l = 2$, $n = 1$ toroidal Ohm mode. The rapid evolution to a poloidally dominant field can be easily visualized by plotting the evolution of the ratio of poloidal to total magnetic energy, as is done in Fig. 4.5. The two scenarios then do not seem so disconnected, as toroidally dominated fields will quickly increase their E_P/E ratio, both via rapid Ohmic dissipation and energy transfer to the poloidal field, until the poloidally dominated regime is reached, from which point the evolution will proceed with stable oscillations until Ohmic dissipation overcomes the whole evolution. For simulations with progressively stronger toroidal fields, more energy will be lost in this stage of rapid Ohmic dissipation, producing oscillations with longer periods when they reach the poloidally dominant regime. In particular, Fig. 4.5 and 4.4 show that for the case that starts with $E_P/E = 0.1$ no clear oscillatory behavior occurs, as Ohmic dissipation quickly becomes dominant.

It is interesting that the final configuration dominated by Ohmic dissipation has a quadrupole toroidal field rather than a dipole which has a slower decay rate. This is due to the fact that the dominant poloidal dipole field acting on itself due to Hall drift produces a quadrupolar toroidal field.

4.1.1 Comparision with Meissner boundary conditions

To check whether the inclusion of superconductor boundary conditions modifies significantly the evolution, I perform four additional simulations with $R_B = 50$, two for each case of $E_P/E = 0.1$ and $E_P/E = 0.9$, with and without Meissner boundary conditions. However, since combinations of the form of Eq. (4.2) will not satisfy the boundary conditions initially, I choose a modified toroidal field given by

$$\boldsymbol{B}_t = (r - r_{min})\hat{\boldsymbol{B}}_{11t} \tag{4.3}$$

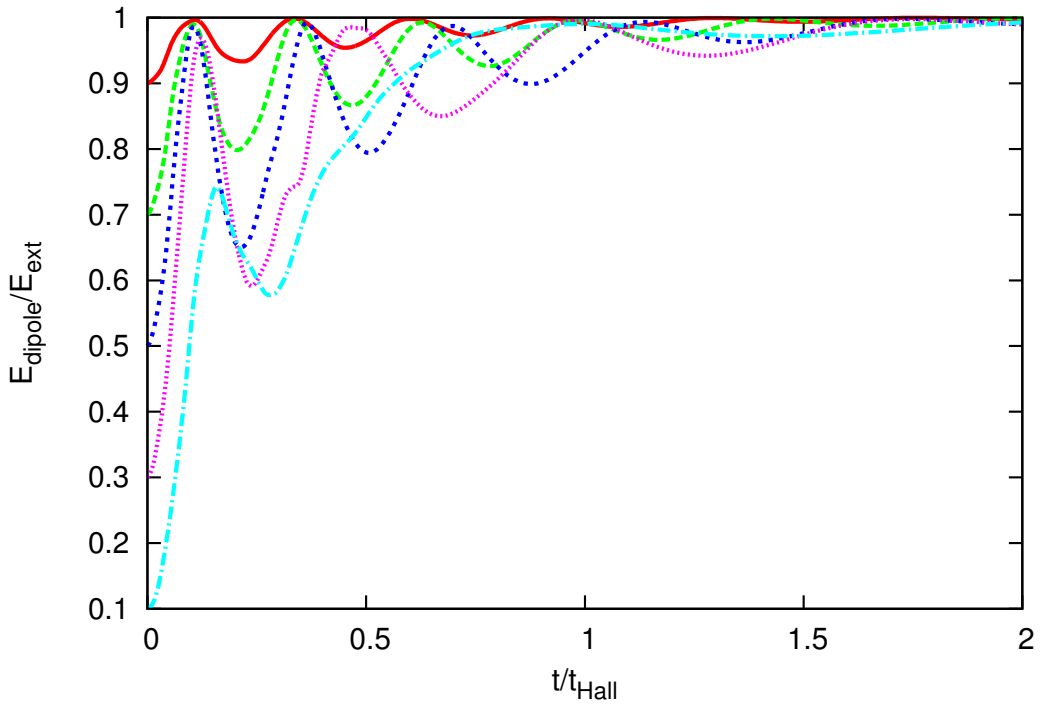

Figure 4.5: Evolution of the ratio E_P/E for simulations with different initial ratios. Predominantly toroidal fields evolve quickly past equipartition to a poloidally dominant field where they follow stable oscilations with the ratio E_P/E going asymptotically to 1. The predominantly toroidal simulation with an initial value $E_P/E = 0.1$ shows a somewhat different behavior, but still evolves to a predominantly poloidal field.

This field has zero radial derivative and zero value at the crust-core interface, and thus, will satisfy the Meissner boundary conditions. I rescale the energy of this field as was done before, and construct the combinations with the energy ratios just mentioned before.

The results shown in Fig. 4.6 show that the evolution on short timescales does not change much, although the simulations with zero boundary conditions have a slightly enhanced energy dissipation. However, for longer timescales where Ohmic dissipation becomes the dominant effect, simulations with Meissner boundary conditions evolve to predominantly toroidal configurations, which consists in the fundamental Ohm mode as shown in Fig. 4.7. This is completely different to the case with zero boundary conditions, where Ohmic dissipation drives the field to a poloidally dominated configuration. The long time it takes to reach this final configuration with Meissner boundary conditions is due to the similarity of the decay rates of the fundamental toroidal mode and the toroidal quadrupole.

Unlike the simulations with zero boundary conditions, where the poloidal field acting on itself caused the toroidal quadrupole to remain in the long run even though it has a faster decay rate, the dominant toroidal mode will not produce a higher poloidal multipole, since the Hall term in the equation for $\partial\alpha/\partial t$ depends on the intensities of both and thus will never dominate over the Ohmic dissipation of the poloidal field.

4.1.2 Symmetry-preserving initial conditions

At this point, the claim that toroidally dominated fields quickly evolve to a poloidally dominated scenario cannot be done in a general sense. This is not only due to the very simplified model of the crust, but also because the conclusions are drawn from a set of scenarios for which the geometry of the field is essentially the same. To extend the analysis, I consider a combination of poloidal and toroidal fields which will evolve preserving the initial symmetries,

$$\boldsymbol{B} = \sqrt{E_P/E}\boldsymbol{B}_{11p} + \sqrt{1 - E_P/E}\boldsymbol{B}_{21t}, \tag{4.4}$$

which is a combination of the fundamental poloidal Ohm mode and a quadrupolar toroidal field. The fact that this field will preserve its symmetry (i.e. α will remain symmetric with respect to the equator and β will remain antisymmetric), is given by the discussion at the end of §2. The results of simulations with $R_B = 100$ for fields of the form of Eq. (4.4)

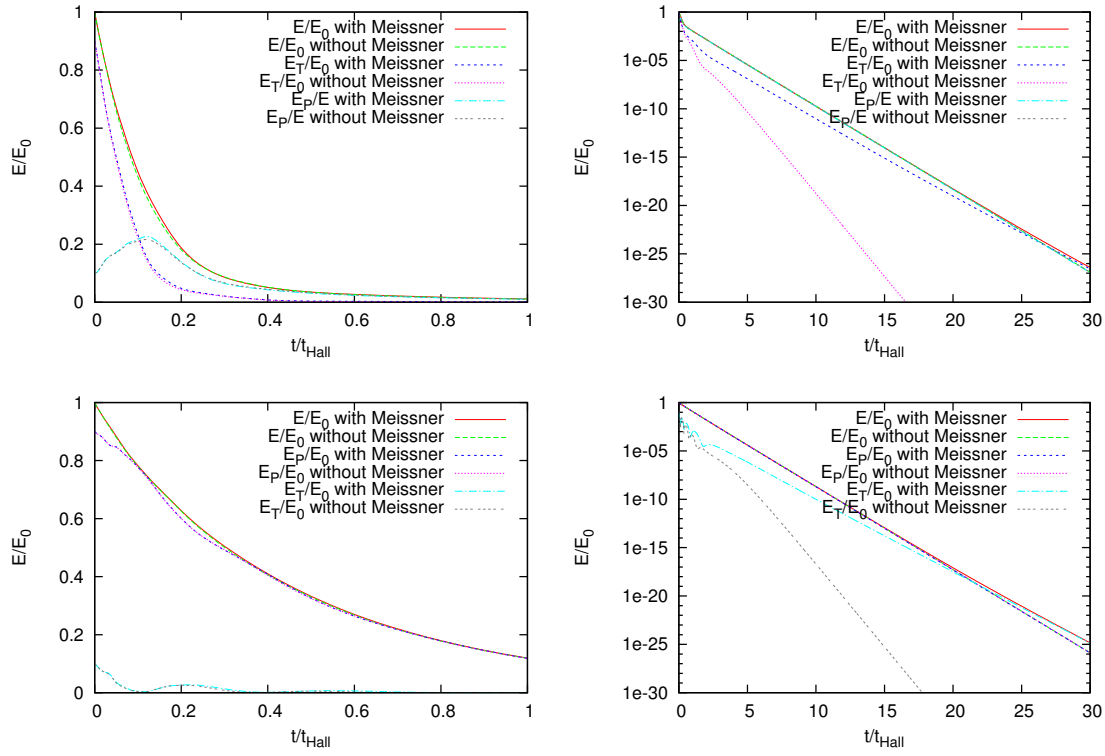

Figure 4.6: Evolution of total, toroidal and poloidal energies with respect to the total initial energy for the toroidally dominant (top 2 plots) and the poloidally dominant (bottom 2 plots) configurations described in §4.1.1, up to $t/t_{Hall} = 30$.

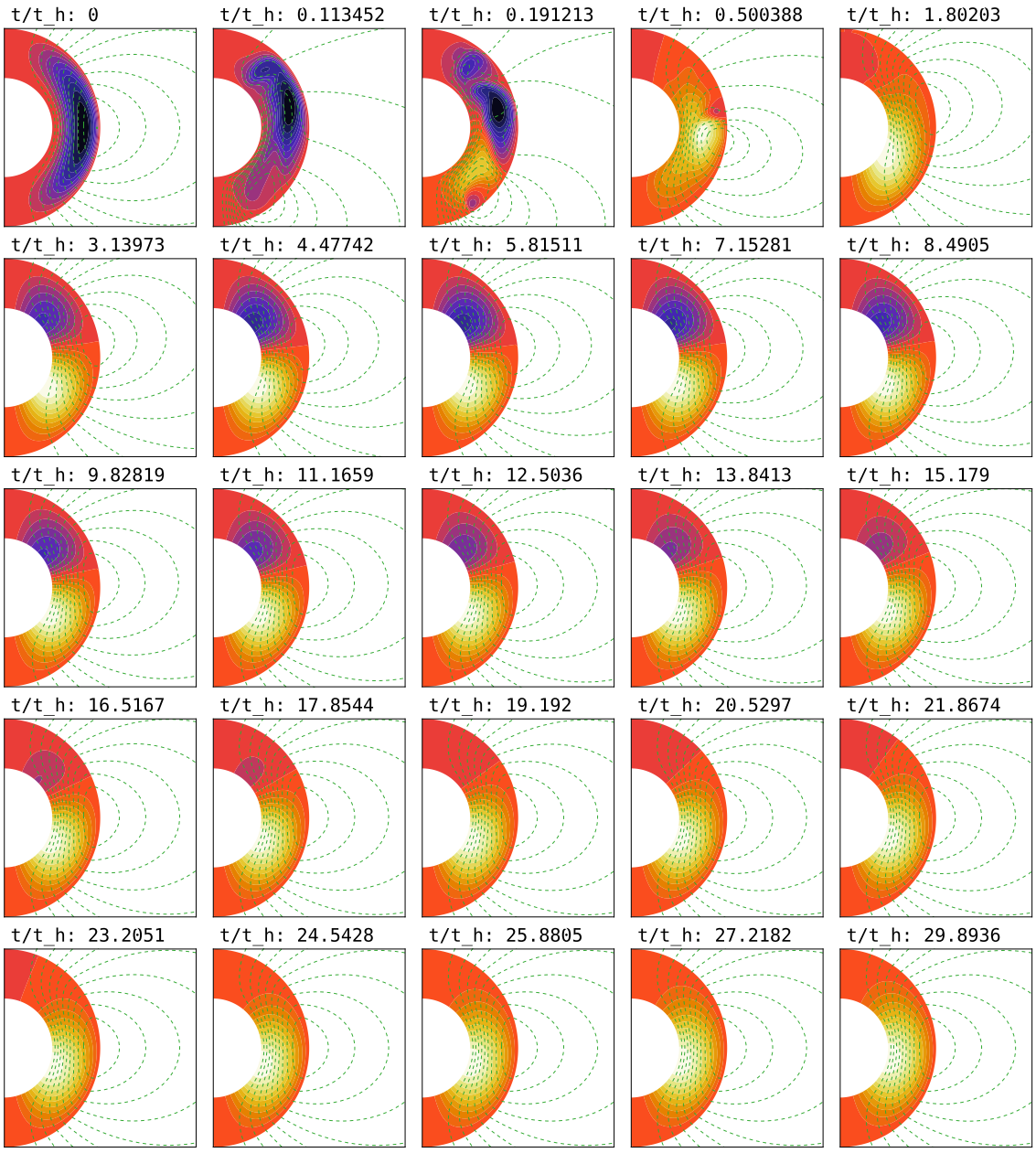

Figure 4.7: Evolution of the toroidally dominated field given in §4.1.1 with Meissner boundary conditions.

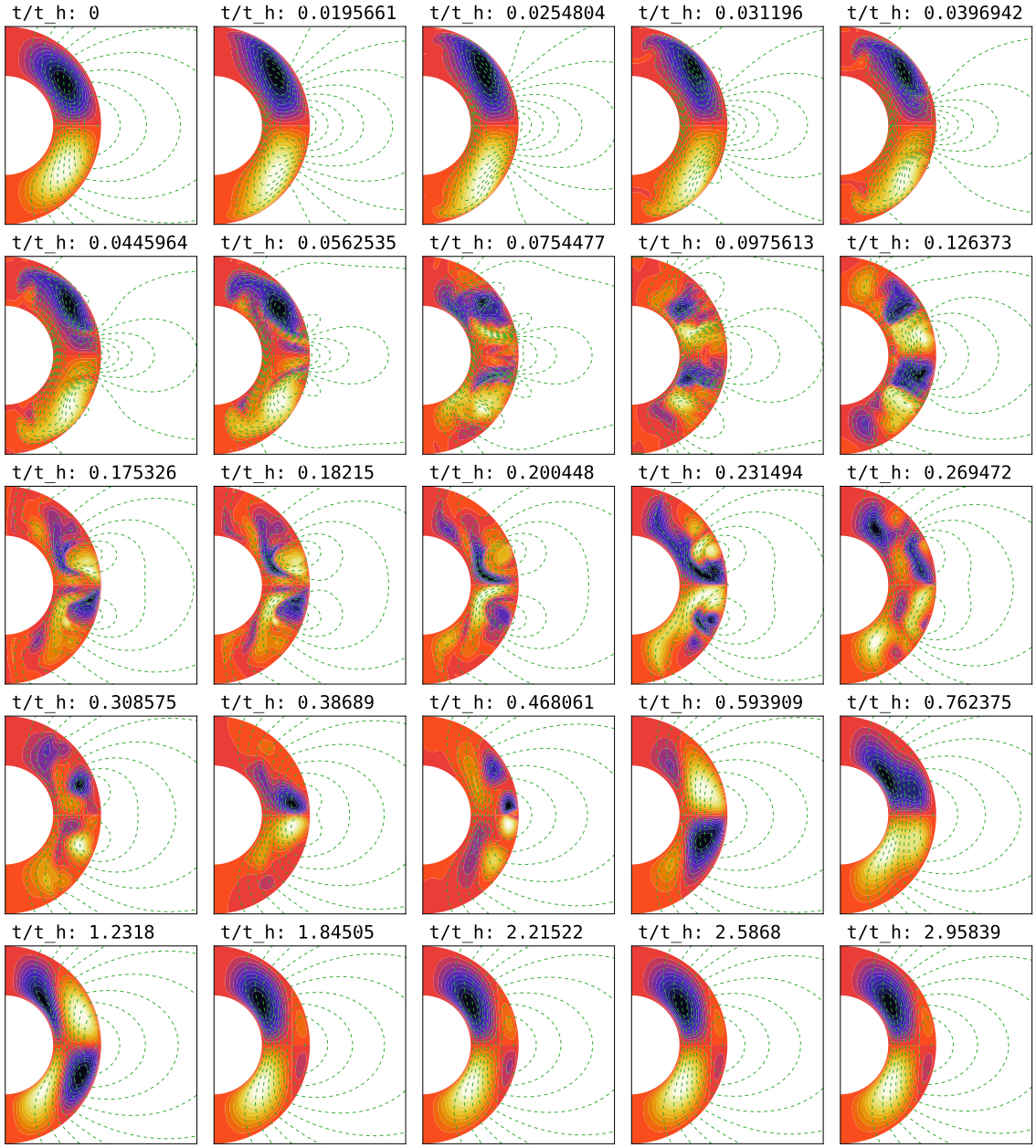

Figure 4.8: Evolution of the field described by Eq. (4.4) with $R_B = 100$, $E_P/E = 0.1$ and zero boundary conditions. The toroidally dominated field rapidly decays, reaching a poloidally dominated regime where some oscilations are observable before the field starts to settle due to Ohmic dissipation.

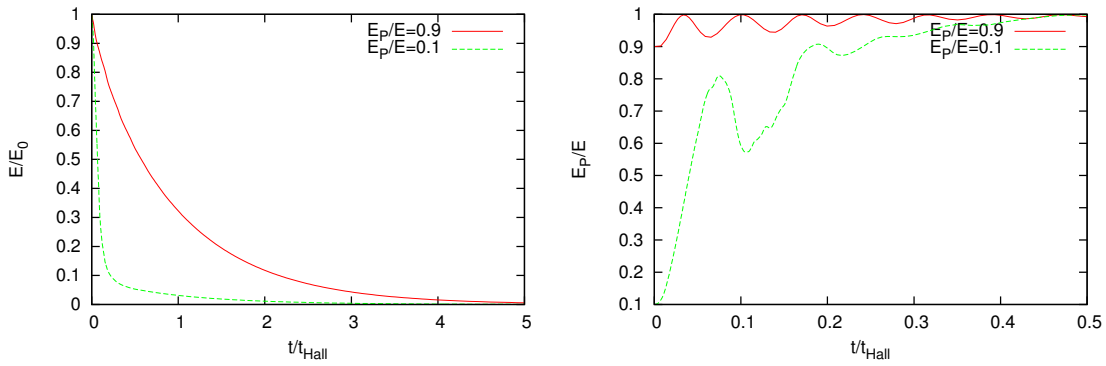

Figure 4.9: Evolution of the field described by Eq. (4.4) for the ratios of poloidal to total energy $E_P/E = 0.1$ and 0.9. The plot on the left shows the evolution of the total energy, while the plot on the right shows the evolution of the ratio of poloidal to total energy. Just as with the previous cases, the toroidally dominated field is affected by rapid Ohmic dissipation and eventually reaches the poloidally dominated regime.

are shown in the plots of Fig. 4.9, and snapshots of the toroidally dominated simulation are shown in Fig. 4.8. The evolution of the fields fits the framework already described for the regimes of either poloidally or toroidally dominated fields, where a poloidally dominant field has stable oscillations, while a toroidally dominant field efficiently loses energy until it reaches a configuration where the poloidal field is dominant. Moreover, simulations mixing $\boldsymbol{B}_{31p}$ and $\boldsymbol{B}_{21t}$ (not shown here) behave just the same, with the case of the poloidally dominated field oscillating without significantly changing its $l = 3$ structure. Other combinations do not retain such a similarity with the initial conditions as they evolve, but they follow the general behavior that initially poloidally dominated fields end up having stable oscillations while initially toroidally dominated fields quickly lose toroidal magnetic field energy until they reach the poloidally dominated regime, which needs not resemble the initial choice of modes used.

The question remains now, if this behaviour is extended in any way to realistic, stably stratified models for the crust.

4.2 Stability of Hall equilibria

In order to study the stability of the Hall equilibrium given by eq. (2.46), I perform simulations for $R_B = 50, 100, 200, 400$. However, a slight numerical problem arose while attempting to perform these simulations. The numerical resolution of $\Delta^*\alpha$ right at the surface depends on the radial derivative which is solved in terms of the multipolar expansion. This expansion was not precise enough, causing a small error in its resolution. When time-evolving $\beta^k_{r_{num-1},j}$, a radial derivative of $\Delta^*\alpha$ is needed, and the small error in its calculation at the surface becomes more important. This is not an issue in the non-equilibrium cases studied in the previous section, however, in the case of a Hall equilibrium, the numerically calculated Hall terms in the evolution equation for β will all be very close to zero expect for points right below the surface, producing a numerical artefact that ends up dominating the evolution. In order to avoid this, the $\beta^k_{r_{num-1},j}$ are evolved by interpolation between the surface and $\beta^k_{r_{num-2},j}$,

$$\beta^k_{N_r-1,j} = \frac{1}{2}\left(\beta^k_{N_r-2,j} + \beta^k_{N_r,j}\right) = \frac{1}{2}\beta^k_{N_r-2,j}, \tag{4.5}$$

where the zero boundary condition at the surface was used. Since in these poloidally dominated cases the toroidal field should not produce steep current sheets at the surface, this approximation should not alter significantly the evolution.

As said in §2.3, the equilibrium field I use is solved using zero boundary conditions at the core-crust interface, and so, I use this boundary condition when evolving this field. In any case, as was shown in §4.1.1, the use of Meissner boundary conditions does not change the early evolution significantly, and only becomes evident at later stages when Ohmic decay becomes dominant, and so, the choice of boundary conditions is not expected to play an important role in the stability of the equilibria.

As the field is affected by Ohmic decay, its structure will be modified, driving it out of equilibrium and, thus, acting as a perturbation. The simplest test that can be done to see if Hall drift plays an important role in modifying the structure of the field is comparing its evolution with and without Hall drift, as is shown in Fig. 4.10, where it can be seen that Hall drift only slightly enhances the rate of energy decay, which in the end is essentially the decay rate for the energy of the fundamental poloidal Ohm mode.

Since the decay rate of the total energy of the field does not seem to be affected

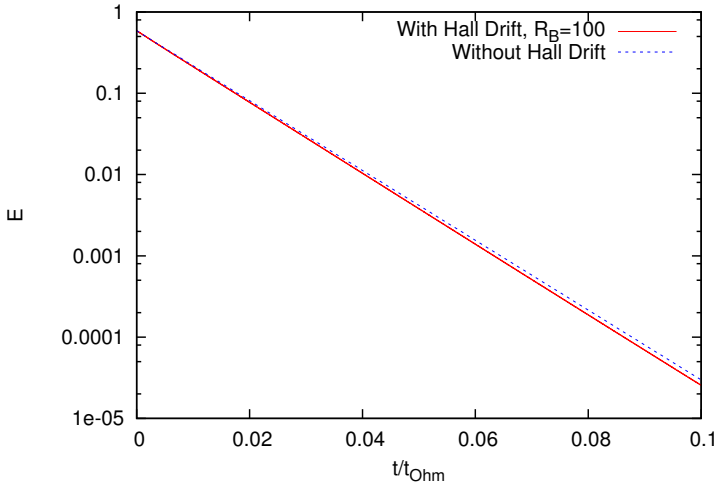

Figure 4.10: Decay of the equilibrium field in a coupled Hall+Ohm case with $R_B = 100$, compared with the case of pure Ohmic decay without Hall drift. It can be seen that the decay timescale is not significantly modified by Hall drift

significantly by the presence of Hall drift, it is necessary to have a more sensitive measure of the departure from the equilibrium field. For this purpose, I consider the time-dependent field $\boldsymbol{B}(\boldsymbol{r}, t)$, the initial equilibrium field $\boldsymbol{B}_{eq}(\boldsymbol{r})$, and the fundamental poloidal Ohm mode $\boldsymbol{B}_{11p}(\boldsymbol{r})$ normalized as

$$\begin{aligned}
\hat{\boldsymbol{B}}(\boldsymbol{r}, t) =& \frac{\boldsymbol{B}(\boldsymbol{r}, t)}{\int_V \left(\boldsymbol{B}(\boldsymbol{r}, t)\right)^2 \, \mathrm{d}\, V}, \\
\hat{\boldsymbol{B}}_{eq}(\boldsymbol{r}) =& \frac{\boldsymbol{B}_{eq}(\boldsymbol{r})}{\int_V \left(\boldsymbol{B}_{eq}(\boldsymbol{r})\right)^2 \, \mathrm{d}\, V}, \\
\hat{\boldsymbol{B}}_{11p}(\boldsymbol{r}) =& \frac{\boldsymbol{B}_{11p}(\boldsymbol{r})}{\int_V \left(\boldsymbol{B}_{11p}(\boldsymbol{r})\right)^2 \, \mathrm{d}\, V},
\end{aligned} \tag{4.6}$$

where V is the volume of all space outside the core, i.e. $r > r_{min}$. The direction of the Ohm field is chosen in such a way that it is equal to the direction of the equilibrium field, i.e. so that $\hat{\boldsymbol{B}}_{11p}$ and $\hat{\boldsymbol{B}}_{eq}$ share the same magnetic north pole.

In terms of these normalized fields, I define the quantities

$$\delta_{eq} = \int_V (\hat{\boldsymbol{B}}(\boldsymbol{r},t) - \hat{\boldsymbol{B}}_{eq}(\boldsymbol{r}))^2 \,\mathrm{d}\,V, \qquad \delta_{ohm} = \int_V (\hat{\boldsymbol{B}}(\boldsymbol{r},t) - \hat{\boldsymbol{B}}_{11p}(\boldsymbol{r}))^2 \,\mathrm{d}\,V, \tag{4.7}$$

where V is just as before the volume outside the crust. These deltas will measure the difference in shape of the time-evolved field with respect to the initial equilibrium field and the fundamental poloidal Ohm mode, to which eventually the system will decay. In order to evaluate the integrals, I split them in the regions inside and outside the star,

$$\delta_{eq} = \int_{V_{crust}} (\hat{\boldsymbol{B}} - \hat{\boldsymbol{B}}_{eq})^2 \,\mathrm{d}\,V + \int_{r>R} (\hat{\boldsymbol{B}}^2 - 2\hat{\boldsymbol{B}}\cdot\hat{\boldsymbol{B}}_{eq} + \hat{\boldsymbol{B}}_{eq}^2) \,\mathrm{d}\,V, \tag{4.8}$$

which, using the same procedure as in §2.1.3 to solve for the energy outside the star results in

$$\delta_{eq} = \int_{V_{crust}} (\hat{\boldsymbol{B}} - \hat{\boldsymbol{B}}_{eq})^2 \,\mathrm{d}\,V + \sum_{l=1}^{\infty} (l+1)\left(|\hat{a}_l|^2 - 2\hat{a}_l\hat{a}_{l,eq} + |\hat{a}_{l,eq}|^2\right), \tag{4.9}$$

where $\hat{a}_l$ and $\hat{a}_{l,eq}$ denote the multipole coefficients of the normalized time-dependent and equilibrium fields respectively. Since the equilibrium and the fundamental Ohm mode are exact dipoles, the final expression for the deltas is

$$\begin{aligned} \delta_{eq} &= \int_{V_{crust}} (\hat{\boldsymbol{B}} - \hat{\boldsymbol{B}}_{eq})^2 \,\mathrm{d}\,V - 4\hat{a}_1\hat{a}_{1,eq} + 2|\hat{a}_{1,eq}|^2 + \sum_{l=1}^{\infty}(l+1)|\hat{a}_l|^2, \\ \delta_{Ohm} &= \int_{V_{crust}} (\hat{\boldsymbol{B}} - \hat{\boldsymbol{B}}_{11p})^2 \,\mathrm{d}\,V - 4\hat{a}_1\hat{a}_{1,11p} + 2|\hat{a}_{1,11p}|^2 + \sum_{l=1}^{\infty}(l+1)|\hat{a}_l|^2. \end{aligned} \tag{4.10}$$

Of course, when numerically computing these values, I restrict the summation up to the maximum multipole L of the simulation.

The first simple test that has to be done is to check the evolution of δ_{eq} and δ_{Ohm} for the equilibrium field subject only to Ohmic dissipation. In this case, I expect the higher modes that compose the field to rapidly decay, leaving only the fundamental Ohm mode. Thus, δ_{Ohm} will start with an initial non-zero value, δ_{eq} will be equal to zero, and with time δ_{Ohm} should asymptotically go to zero, while δ_{eq} should asymptotically go to the value δ_{Ohm} had initially. This is shown in Fig. 4.11, where it can be seen that around

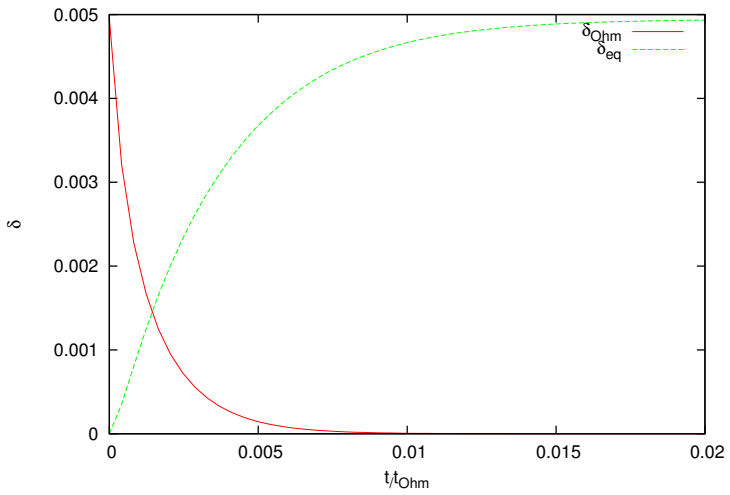

Figure 4.11: Evolution of δ_{Ohm} and δ_{eq} in the case with no Hall drift. Note that the values are much smaller than unity, indicating that the equilibrium field is very similar to the fundamental Ohm mode.

$t/t_{Ohm} \sim 0.02$ the equilibrium field has essentially decayed to the fundamental Ohm mode.

Now, adding Hall drift to the picture, Fig. 4.12 shows the evolution of δ_{eq} and δ_{Ohm} for different values of R_B. The most obvious changes with respect to the previous results are that the asymptotic evolution to the fundamental Ohm mode takes much longer, and that a departure from both fields used as reference happens during the initial stages of evolution. This departure scales with t_{Ohm}, meaning this that as I change R_B this part of the evolution remains nearly unchanged when plotted as a function of t/t_{Ohm}, so it is not likely to be an instability driven by Hall drift. Small oscillations can be seen on top of this curve, which gradually decrease their intensity and, most importantly, have periods that scale with t_{Hall}. In any case, the departure from the equilibrium is very small, as significant perturbations to the structure would produce deltas much closer to unity.

In order to better understand what this digression both from the initial equilibrium field and the final fundamental Ohm mode means, I construct a simple spectral model of

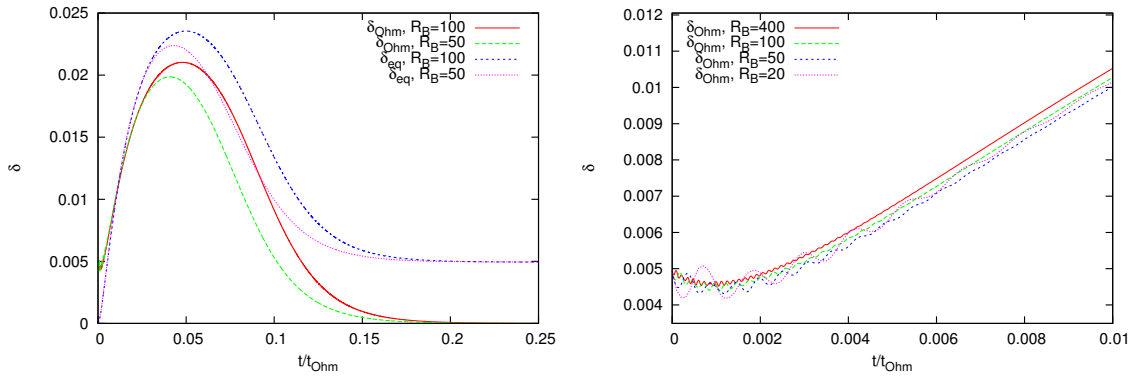

Figure 4.12: (left) Evolution of δ_{Ohm} and δ_{eq} in the case with Hall drift. For different values of $R_B = 50, 100$. (right) Closeup to the beginning of the evolution, showing δ_{Ohm} for $R_B = 50, 100, 200, 400$. The rise scales with t_{Ohm} while the small oscilations at the beginning of the simulation scale with t_{Hall}.

the system in terms of the first few Ohmic modes,

$$\begin{aligned}\boldsymbol{B}(t) \simeq\ & a_{11}(t)\hat{\boldsymbol{B}}_{11p} + a_{21}(t)\hat{\boldsymbol{B}}_{21p} + a_{31}(t)\hat{\boldsymbol{B}}_{31p} \\ & + a_{13}(t)\hat{\boldsymbol{B}}_{13p} + a_{23}(t)\hat{\boldsymbol{B}}_{23p} + a_{33}(t)\hat{\boldsymbol{B}}_{33p} \\ & + b_{12}(t)\hat{\boldsymbol{B}}_{12t} + b_{22}(t)\hat{\boldsymbol{B}}_{22t} + b_{32}(t)\hat{\boldsymbol{B}}_{32t}\end{aligned} \tag{4.11}$$

where the Ohmic modes $\hat{\boldsymbol{B}}_{nlp}$ and $\hat{\boldsymbol{B}}_{nlt}$ are the ones described in §2.2 for zero boundary conditions, with the p and t subscripts denoting poloidal and toroidal modes respectively, normalized in the same way as in Eq. (4.6). These modes are then orthonormal, and the energy of each component is simply its coefficient a_{nl} or b_{nl} squared and multiplied by $(8\pi)^{-1}$. The exclusion of toroidal modes with $l = 1, 3$ and poloidal modes with $l = 2$ is done because of the symmetry properties discussed at the end of §2, which indicate that for this field α will remain symmetric with respect to the equator, while β will always be antisymmetric. These symmetries are explicitly seen in the simulations, so if any symmetry-breaking instability exists, which could be induced because the numerical initial conditions will not be perfectly symmetric (or antisymmetric), it is not observed and thus I ignore it in this analysis.

Just as before, the direction of the fields is relevant, and it should be defined in an

unambiguous way. I will consider all 6 poloidal modes chosen in such a way that they are aligned with the equilibrium field (which means $B_r(r = R, \theta = 0) > 0$) and all toroidal $l = 2$ modes in such a way that right below the surface of the Northern hemisphere ($0 < \theta < \pi/2$) the azimuthal component B_ϕ is positive. Decomposing the equilibrium field in terms of the Ohm modes so defined I get

$$\boldsymbol{B}_{eq} \simeq 3.840\hat{\boldsymbol{B}}_{11p} - 0.224\hat{\boldsymbol{B}}_{21p} + 0.134\hat{\boldsymbol{B}}_{31p} - 0.051\hat{\boldsymbol{B}}_{41p}, \tag{4.12}$$

where also the component on the fourth radial mode was included for comparison. If the energy of the equilibrium field is computed, and compared with the energy of the dipole, it is seen that $\sim 99.5\%$ of the energy comes from it while the other three components shown add up a $\sim 0.48\%$ of the total energy. It seems reasonable to assume that the remaining components will not affect the evolution significantly, but even so, for simplicity I do not take the a_{41} coefficient into account in my model, although for the initial condition it is not much smaller than the a_{21} or the a_{31} components.

I now decompose the dimensionless version of Eq. (1.4) with constant electron density and resistivity,

$$\frac{\partial \boldsymbol{B}}{\partial t} = -\nabla \times ([\nabla \times \boldsymbol{B}] \times \boldsymbol{B}) - R_B^{-1} \nabla \times (\nabla \times \boldsymbol{B}), \tag{4.13}$$

in terms of the Ohm modes. The Ohmic term is trivial, but the Hall term requires numerical integrations to obtain all the relevant terms. Since a_{11} is much larger than all other terms at the beginning, and the simulations show that the structure of the field does not change substantially, I ignore all non-linear terms that do not contain this coefficient. The Hall

term is then approximated as

$$\begin{aligned}
-\nabla\times([\nabla\times\boldsymbol{B}]\times\boldsymbol{B}) \simeq & -a_{11}^2\nabla\times([\nabla\times\hat{\boldsymbol{B}}_{11p}]\times\hat{\boldsymbol{B}}_{11p}) \\
& -a_{11}a_{21}\nabla\times([\nabla\times\hat{\boldsymbol{B}}_{11p}]\times\hat{\boldsymbol{B}}_{21p}+[\nabla\times\hat{\boldsymbol{B}}_{21p}]\times\hat{\boldsymbol{B}}_{11p}) \\
& -a_{11}a_{31}\nabla\times([\nabla\times\hat{\boldsymbol{B}}_{11p}]\times\hat{\boldsymbol{B}}_{31p}+[\nabla\times\hat{\boldsymbol{B}}_{31p}]\times\hat{\boldsymbol{B}}_{11p}) \\
& -a_{11}a_{13}\nabla\times([\nabla\times\hat{\boldsymbol{B}}_{11p}]\times\hat{\boldsymbol{B}}_{13p}+[\nabla\times\hat{\boldsymbol{B}}_{13p}]\times\hat{\boldsymbol{B}}_{11p}) \\
& -a_{11}a_{23}\nabla\times([\nabla\times\hat{\boldsymbol{B}}_{11p}]\times\hat{\boldsymbol{B}}_{23p}+[\nabla\times\hat{\boldsymbol{B}}_{23p}]\times\hat{\boldsymbol{B}}_{11p}) \\
& -a_{11}a_{33}\nabla\times([\nabla\times\hat{\boldsymbol{B}}_{11p}]\times\hat{\boldsymbol{B}}_{33p}+[\nabla\times\hat{\boldsymbol{B}}_{33p}]\times\hat{\boldsymbol{B}}_{11p}) \\
& -a_{11}b_{12}\nabla\times([\nabla\times\hat{\boldsymbol{B}}_{12t}]\times\hat{\boldsymbol{B}}_{11p}) \\
& -a_{11}b_{22}\nabla\times([\nabla\times\hat{\boldsymbol{B}}_{22t}]\times\hat{\boldsymbol{B}}_{11p}) \\
& -a_{11}b_{32}\nabla\times([\nabla\times\hat{\boldsymbol{B}}_{32t}]\times\hat{\boldsymbol{B}}_{11p}).
\end{aligned} \tag{4.14}$$

For the initial values $a_{11,i} = 3.840$, $a_{21,i} = -0.224$, and $a_{31,i} = 0.134$, the Hall term is approximately zero,

$$\begin{aligned}
0 \simeq & -a_{11,i}^2\nabla\times([\nabla\times\hat{\boldsymbol{B}}_{11p}]\times\hat{\boldsymbol{B}}_{11p}) \\
& -a_{11,i}a_{21,i}\nabla\times([\nabla\times\hat{\boldsymbol{B}}_{11p}]\times\hat{\boldsymbol{B}}_{21p}+[\nabla\times\hat{\boldsymbol{B}}_{21p}]\times\hat{\boldsymbol{B}}_{11p}). \\
& -a_{11,i}a_{31,i}\nabla\times([\nabla\times\hat{\boldsymbol{B}}_{11p}]\times\hat{\boldsymbol{B}}_{31p}+[\nabla\times\hat{\boldsymbol{B}}_{31p}]\times\hat{\boldsymbol{B}}_{11p})
\end{aligned} \tag{4.15}$$

Defining $\gamma_1(t)$, $\gamma_2(t)$ and $\gamma_3(t)$ as

$$a_{11}(t) = \gamma_1(t)a_{11,i}, \quad a_{21}(t) = (\gamma_1(t)+\gamma_2(t))a_{21,i} \quad a_{31}(t)(\gamma_1(t)+\gamma_3(t))a_{31,i}, \tag{4.16}$$

and combining this with Eqs. (4.14) and (4.15), the approximation for the Hall term can

be written as

$$\begin{aligned}
-\nabla\times([\nabla\times\boldsymbol{B}]\times\boldsymbol{B}) \simeq & -a_{11,i}a_{21,i}\gamma_1\gamma_2\nabla\times([\nabla\times\hat{\boldsymbol{B}}_{11p}]\times\hat{\boldsymbol{B}}_{21p}+[\nabla\times\hat{\boldsymbol{B}}_{21p}]\times\hat{\boldsymbol{B}}_{11p})\\
& -a_{11,i}a_{31,i}\gamma_1\gamma_3\nabla\times([\nabla\times\hat{\boldsymbol{B}}_{11p}]\times\hat{\boldsymbol{B}}_{31p}+[\nabla\times\hat{\boldsymbol{B}}_{31p}]\times\hat{\boldsymbol{B}}_{11p})\\
& -a_{11}a_{13}\nabla\times([\nabla\times\hat{\boldsymbol{B}}_{11p}]\times\hat{\boldsymbol{B}}_{13p}+[\nabla\times\hat{\boldsymbol{B}}_{13p}]\times\hat{\boldsymbol{B}}_{11p})\\
& -a_{11}a_{23}\nabla\times([\nabla\times\hat{\boldsymbol{B}}_{11p}]\times\hat{\boldsymbol{B}}_{23p}+[\nabla\times\hat{\boldsymbol{B}}_{23p}]\times\hat{\boldsymbol{B}}_{11p})\\
& -a_{11}a_{33}\nabla\times([\nabla\times\hat{\boldsymbol{B}}_{11p}]\times\hat{\boldsymbol{B}}_{33p}+[\nabla\times\hat{\boldsymbol{B}}_{33p}]\times\hat{\boldsymbol{B}}_{11p})\\
& -a_{11}b_{12}\nabla\times([\nabla\times\hat{\boldsymbol{B}}_{12t}]\times\hat{\boldsymbol{B}}_{11p})\\
& -a_{11}b_{22}\nabla\times([\nabla\times\hat{\boldsymbol{B}}_{22t}]\times\hat{\boldsymbol{B}}_{11p})\\
& -a_{11}b_{32}\nabla\times([\nabla\times\hat{\boldsymbol{B}}_{32t}]\times\hat{\boldsymbol{B}}_{11p}).
\end{aligned} \tag{4.17}$$

Defining δ_2 and δ_3 as

$$\delta_2=\left(a_{21}-a_{11}\frac{a_{21,i}}{a_{11,i}}\right),\qquad \delta_3=\left(a_{31}-a_{11}\frac{a_{31,i}}{a_{11,i}}\right), \tag{4.18}$$

Eq. (4.17) can be written as

$$\begin{aligned}
-\nabla\times([\nabla\times\boldsymbol{B}]\times\boldsymbol{B}) \simeq & -a_{11}\delta_2\nabla\times([\nabla\times\hat{\boldsymbol{B}}_{11p}]\times\hat{\boldsymbol{B}}_{21p}+[\nabla\times\hat{\boldsymbol{B}}_{21p}]\times\hat{\boldsymbol{B}}_{11p})\\
& -a_{11}\delta_3\nabla\times([\nabla\times\hat{\boldsymbol{B}}_{11p}]\times\hat{\boldsymbol{B}}_{31p}+[\nabla\times\hat{\boldsymbol{B}}_{31p}]\times\hat{\boldsymbol{B}}_{11p})\\
& -a_{11}a_{13}\nabla\times([\nabla\times\hat{\boldsymbol{B}}_{11p}]\times\hat{\boldsymbol{B}}_{13p}+[\nabla\times\hat{\boldsymbol{B}}_{13p}]\times\hat{\boldsymbol{B}}_{11p})\\
& -a_{11}a_{23}\nabla\times([\nabla\times\hat{\boldsymbol{B}}_{11p}]\times\hat{\boldsymbol{B}}_{23p}+[\nabla\times\hat{\boldsymbol{B}}_{23p}]\times\hat{\boldsymbol{B}}_{11p})\\
& -a_{11}a_{33}\nabla\times([\nabla\times\hat{\boldsymbol{B}}_{11p}]\times\hat{\boldsymbol{B}}_{33p}+[\nabla\times\hat{\boldsymbol{B}}_{33p}]\times\hat{\boldsymbol{B}}_{11p})\\
& -a_{11}b_{12}\nabla\times([\nabla\times\hat{\boldsymbol{B}}_{12t}]\times\hat{\boldsymbol{B}}_{11p})\\
& -a_{11}b_{22}\nabla\times([\nabla\times\hat{\boldsymbol{B}}_{22t}]\times\hat{\boldsymbol{B}}_{11p})\\
& -a_{11}b_{32}\nabla\times([\nabla\times\hat{\boldsymbol{B}}_{32t}]\times\hat{\boldsymbol{B}}_{11p}).
\end{aligned} \tag{4.19}$$

I decompose this in terms of the Ohmic modes by numerical integration, after which, including the Ohmic dissipation terms, Eq. (4.13) turns into nine differential equations for

the coefficients a_{nl} and b_{nl},

$$\begin{aligned}
\dot{a}_{11} =& -\lambda_{11p}a_{11} + 1.927a_{11}b_{12} - 1.555a_{11}b_{22} - 0.450a_{11}b_{32} \\
\dot{a}_{21} =& -\lambda_{21p}a_{21} + 28.964a_{11}b_{12} + 23.269a_{11}b_{22} - 6.559a_{11}b_{32} \\
\dot{a}_{31} =& -\lambda_{31p}a_{31} - 6.394a_{11}b_{12} + 77.274a_{11}b_{22} + 67.760a_{11}b_{32} \\
\dot{a}_{13} =& -\lambda_{13p}a_{13} + 13.937a_{11}b_{12} - 5.771a_{11}b_{22} - 1.466a_{11}b_{32} \\
\dot{a}_{23} =& -\lambda_{23p}a_{23} + 2.930a_{11}b_{12} + 55.121a_{11}b_{22} - 15.401a_{11}b_{32} \\
\dot{a}_{33} =& -\lambda_{33p}a_{33} + 0.578a_{11}b_{12} + 35.594a_{11}b_{22} + 121.469a_{11}b_{32} \\
\dot{b}_{12} =& -\lambda_{12t}b_{12} - 27.741a_{11}\delta_2 + 6.172a_{11}\delta_3 - 11.268a_{11}a_{13} - 4.786a_{11}a_{23} - 0.242a_{11}a_{33} \\
\dot{b}_{22} =& -\lambda_{22t}b_{22} - 24.332a_{11}\delta_2 - 76.529a_{11}\delta_3 + 3.642a_{11}a_{13} - 53.480a_{11}a_{23} - 36.763a_{11}a_{33} \\
\dot{b}_{32} =& -\lambda_{32t}b_{32} + 7.124a_{11}\delta_2 - 68.440a_{11}\delta_3 + 0.925a_{11}a_{13} + 14.494a_{11}a_{23} - 120.394a_{11}a_{33},
\end{aligned} \tag{4.20}$$

where $\lambda = R_B^{-1}k^2$, with the k given for each mode in §2.2. This set of equations can be solved numerically via the forward Euler method. Fig. 4.13 shows some results for δ_{Ohm} using $R_B = 100, 200$, and the corresponding values from the full-fledged simulations are included for comparison. Although it is evident that the quantitative agreement is not very good, with the simplified model producing a maximum δ_{Ohm} that is only half that seen in the simulations, the qualitative agreement is very good. Both the rise that scales with t_{Ohm} and the oscillations that scale with t_{Hall} can be clearly seen, and the frequency of the oscillations seems to fit that of the full simulation. Moreover, since the model has a complete decomposition of the fields I can see exactly what modes are responsible for this rise of the deltas, and it turns out that a strong octupolar component develops.

Going back to the simulations to verify the presence of this octupolar component, Fig. 4.14 shows the evolution of the ratio of external energy contained in the octupole to total external energy. Clearly there is a rise that scales with t_{Ohm}, and although the octupole only reaches about 3% of the total external energy, it is enough to explain the rise in δ_{eq} and δ_{Ohm}.

Although this model helps understand what is going on, it is not much less of a black box than the original simulation. However, I have seen that the octupole component play a crucial role in the evolution. In order to get more information from Eq. (4.20), I add further simplifications, first of all reducing the number of modes used to a_{11}, a_{21}, b_{12}, and a_{13}. No fewer modes than this could possibly explain the evolution. Ignoring also the

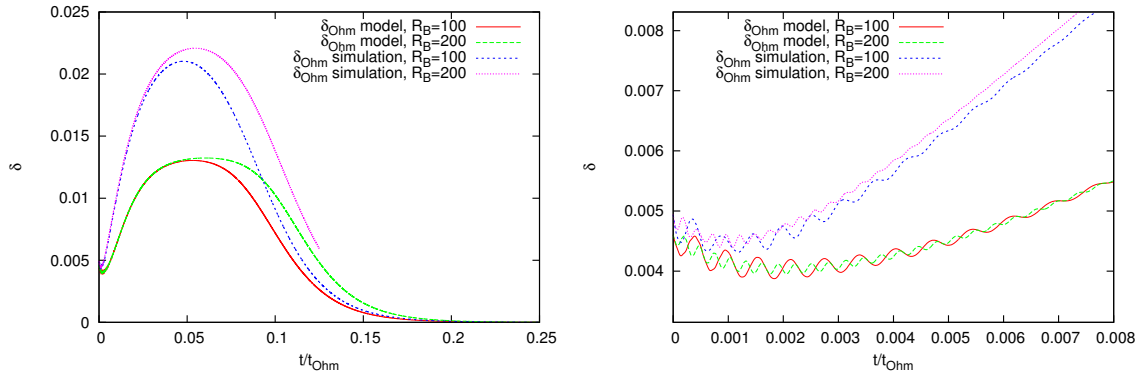

Figure 4.13: (left) Evolution of δ_{Ohm} and δ_{eq} with the simple few-modes model, compared to the results from the full fledged simulations. (right) Close-up to the beginning of the simulation.

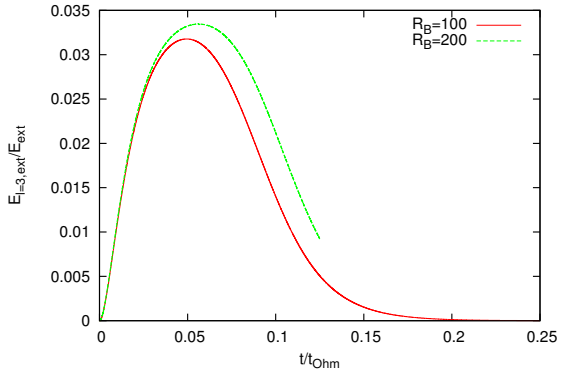

Figure 4.14: Evolution of the ratio of external energy contained in the octupole to total external energy in the simulations with $R_B = 100, 200$.

effects of Ohmic dissipation to study only the effect of the Hall term, I obtain a much smaller and simpler system of equations

$$\begin{aligned}\dot{a}_{11} =& 1.927 a_{11} b_{12} \\ \dot{a}_{21} =& 28.964 a_{11} b_{12} \\ \dot{a}_{13} =& 13.937 a_{11} b_{12} \\ \dot{b}_{12} =& -27.741 a_{11} \delta_2 - 11.268 a_{11} a_{13}.\end{aligned} \tag{4.21}$$

I combine the first two equations in order to produce an equation for $\dot{\delta}_2$ to use instead of the equation for $\dot{a}_{12}$,

$$\dot{\delta}_2 = 28.964 a_{11} b_{12} - 1.927 a_{11} b_{12} \frac{a_{21,i}}{a_{11,i}} \tag{4.22}$$

$$= 29.076 a_{11} b_{12}. \tag{4.23}$$

The final approximation I make is to assume a_{11} constant. This should be descriptive of the behaviour of the system at the beginning of the evolution, and leaves me with a 3×3 system of differential equations,

$$\begin{pmatrix} \dot{\delta}_2 \\ \dot{a}_{13} \\ \dot{b}_{12} \end{pmatrix} = a_{11} \begin{pmatrix} 0 & 0 & 29.076 \\ 0 & 0 & 13.937 \\ -27.741 & -11.268 & 0 \end{pmatrix} \begin{pmatrix} \delta_2 \\ a_{13} \\ b_{12} \end{pmatrix}. \tag{4.24}$$

This system of equations, describing evolution purely through Hall drift around the equilibrium, has two imaginary eigenvalues $\pm 31.043 a_{11} i$, which describe oscillations with a period $0.209 a_{11}^{-1} t_{Hall}$, resulting for the initial value of a_{11} in a period of $0.054 t_{Hall}$, which is close to the actual period of the observed oscilations. The system also has a zero eigenvalue, with solutions that do not evolve in time,

$$b_{12} = 0, \qquad -27.741 \delta_2 - 11.268 a_{13} = 0. \tag{4.25}$$

What this means is that, if I slightly modify the equilibrium field in such a way that this relation is satisfied, the Hall term will be zero (at least in this approximation to the full effect). This seems to be an explanation for the evolution of δ_{eq} and δ_{Ohm}: As Ohmic dissipation modifies the equilibrium field, oscillations will happen around close-by

equilibria, where the octupole component increases in order to compensate the change in δ_2, which is due to the faster dissipation of the $n = 2, l = 1$ component. Eventually, however, Hall drift will become unimportant, and Ohmic dissipation will drive the magnetic field configuration to the fundamental Ohm mode.

Chapter 5

Conclusions

Although Hall drift was proposed as a relevant mechanism for magnetic field evolution in neutron stars more than two decades ago, theoretical results on its effects have not been very conclusive. The non-linear nature of this process has made analytical studies of it very complicated, and numerical simulations have become essential to acquire a better understanding of it.

In this thesis, a finite-difference code has been developed to study the evolution of axially symmetric magnetic fields in neutron star crusts through the combined effects of Hall drift and Ohmic diffusion. The code was tested by checking if it properly reproduced Ohmic decay modes, and comparing the results for the evolution of purely toroidal fields with previous work by Urpin and Shalybkov (1991). Also, Jaime Hoyos, a collaborator of us, had access to the code used by Hollerbach and Rüdiger (2002). Identical simulations were done with both codes, showing a remarkable agreement. Unlike most of the previous simulations implemented, I have properly implemented boundary conditions for the crust-core interface in the case that magnetic field is completely expelled from the interior due to the Meissner effect.

Two different problems were treated with this code, both in the simplified model of constant electron density and resistivity. The first of these, the evolution of either predominantly poloidal or predominantly toroidal fields was treated by Kojima and Kisaka (2012), who showed that a predominantly toroidal field is affected by rapid Ohmic dissipation, transfering energy to the poloidal mode in the process. In contrast, a poloidally dominant configuration would evolve through periodic oscillations, only slightly enhancing

decay. I performed a more detailed analysis of this, checking that after the strong field dissipation happens on a toroidally dominant field, it transitions to stable oscillations in a predominantly poloidal configuration. Most of the tests were performed using a combination of the fundamental poloidal and toroidal Ohm modes, but further exploration on more complex geometries showed that the process has a more general validity. Inclusion of Meissner boundary conditions did not have an important impact on the early evolution, but significantly affected the evolution when Ohmic decay became relevant. Whether this behaviour that separates poloidally and toroidally dominated fields is also present in realistic stratified models of neutron stars, remains to be seen. Even if Hall drift produces structure on smaller scales, this may happen in the innermost regions of the crust, where Ohmic dissipation will not do much unless the structures continue cascading to smaller scales. Some very preliminary simulations with stratified electron density, which are not discussed in this thesis, seems to indicate that this is effectively what happens.

The second problem concerned the stability of a known, an analytically obtained, purely poloidal Hall equilibrium. This field was evolved using the developed code, letting Ohmic diffusion act as a natural perturbation to drive the system away from equilibrium. Even if the equilibrium was stable, the continuous effect of Ohmic decay would have been expected to produce progressively larger perturbations, but on the contrary, a slow departure from the initial equilibrium was observed, which scaled with the Ohmic timescale, and had oscillations of progressively smaller amplitude. Construction of a simple spectral model using Ohm modes showed that a strong octupole component was developed, and closer inspection of the model allowed me to see that this equilibrium is not isolated and has close-by points for which the Hall term is also zero, at least in an approximate sense considering the approximations done. This allows the field to adjust to external perturbations, only slightly modifying its structure, and avoiding large-amplitude variations until Ohmic decay becomes dominant. However, this situation may only be present in this axially symmetric case, as the inclusion of the extra dimension could cause a host of instabilities not observable in my model.

If similar stable equilibrium configurations exist for stratified stars, and supposing that these do not become unstable when the assumption of axial simmetry is removed, it would have very important consequences for the observational properties of magnetars. Objects with similar field strengths could be very different, behaving as very active SGRs if the initial field is too far away from an equilibrium configuration, or as relatively quiescent

and bright AXPs in the opposite case. The analysis done for this thesis should then be extended to models with a realistic electron density profile in order to see if the conclusion holds.

Currently, the work developed in this thesis constitutes a first step towards a more complete picture of magnetic field evolution in neutron stars, and much more work can be done on top of it. Starting first by purely technical details, the numerical methods used are not very elaborate, and a much better precision and stability might be achievable by using, for instance, methods that are second order in time. With respect to physical problems, the assumption that the field is restricted to the crust could be dropped, allowing for magnetic field evolution inside the core of the star. Relating to the study of field stability, extending the code to three dimensions might prove particularly useful, in particular considering that full 3D studies of this problem are practically inexistent (for instance, Wareing and Hollerbach (2010) deals with 3D simulations done on periodic cartesian boxes). Moreover, in ordinary MHD the instabilities of similar field configurations are non-axisymmetric (Tayler (1973), Markey and Tayler (1973)), and if this holds true for Hall MHD too, then 3D simulations would be essential to perform an stability analysis.

References

D. Bhattacharya and E. van den Heuvel. Formation and evolution of binary and millisecond radio pulsars. *Physics Reports*, 203:1–124, 1991.

D. Bhattacharya, R. Wijers, J. Hartman, and F. Verbunt. On the decay of the magnetic fields of single radio pulsars. *A&A*, 254:192–212, 1992.

A. Cumming, P. Arras, and E. Zweibel. Magnetic field evolution in neutron star crusts due to the Hall effect and Ohmic decay. *ApJ*, 609:999–1017, 2004.

C. Faucher-Giguère and V. Kaspi. Birth and evolution of isolated radio pulsars. *ApJ*, 643: 332–355, 2006.

U. Geppert and J. Pons. Magnetic field dissipation in neutron star crusts: from magnetars to isolated neutron stars. *A&A*, 470:303–315, 2007.

P. Goldreich and A. Reisenegger. Magnetic field decay in isolated neutron stars. *ApJ*, 395: 250–258, 1992.

R. Hollerbach and G. Rüdiger. The influence of Hall drift on the magnetic fields of neutron stars. *MNRAS*, 337:216–224, 2002.

R. Hollerbach and G. Rüdiger. Hall drift in the stratified crusts of neutron stars. *MNRAS*, 347:1273–1278, 2004.

P.B. Jones. Neutron star magnetic field decay - Hall drift and Ohmic diffusion. *MNRAS*, 233:875–885, 1988.

V. Kaspi, F. Camilo, A. Lyne, R. Manchester, J. Bell, N. D'Amico, N. McKay, and F. Crawford. Discovery of two high-magnetic-field radio pulsars. *arXiv:astro-ph/9912281*, 1999.

Y. Kojima and S. Kisaka. Magnetic field decay with Hall drift in neutron star crusts. *MNRAS*, 421:2722–2730, 2012.

P. Marchant, A. Reisenegger, and T. Akgün. Revisiting the Flowers-Ruderman instability of magnetic stars. *MNRAS*, 415:2426–2438, 2011.

P. Markey and R. Tayler. The adiabatic stability of stars containing magneticfields-ii. poloidal fields. *MNRAS*, 163:77, 1973.

S. Mereghetti. The strongest cosmic magnets: soft gamma-ray repeaters and anomalous x-ray pulsars. *The Astronomy and Astrophysics Review*, 15:225–287, 2008.

R. Narayan and J. Ostriker. Pulsars populations and their evolution. *ApJ*, 352:222–246, 1990.

J. Ostriker and J. Gunn. On the nature of pulsars. i. theory. *ApJ*, 157, 1969.

J. Pons, J. Miralles, and U. Geppert. Magneto-thermal evolution of neutron stars. *A&A*, 496:207–216, 2009.

A. Reisenegger, R. Benguria, J.P. Prieto, P.A. Araya, and D. Lai. Hall drift of axisymmetric magnetic fields in solid neutron-star matter. *A&A*, 472:233–240, 2007.

D.A. Shalybkov and V.A. Urpin. The Hall effect and the decay of magnetic fields. *A&A*, 321:685–690, 1997.

S. Shapiro and S. Teukolsky. *Black holes, white dwarfs and neutron stars*. 1983.

R. Tayler. The adiabatic stability of stars containing magnetic fields-i.toroidal fields. *MNRAS*, 161:365, 1973.

C. Thompson and R. Duncan. Neutron star dynamos and the origins of pulsar magnetism. *ApJ*, 408:194–217, 1993.

C. Thompson and R. Duncan. The soft gamma repeaters as very strongly magnetized neutron stars - i. radiative mechanism for outbursts. *MNRAS*, 275:255–300, 1995.

C. Thompson and R. Duncan. The soft gamma repeaters as very strongly magnetized neutron stars. ii. quiescent neutrino, x-ray, and alfven wave emission. *ApJ*, 473:322, 1996.

C. Thompson, R. Duncan, P. Woods, C. Kouveliotou, M. Finger, and J. van Paradjis. Physical mechanisms for the variable spin-down and light curve of sgr 1900+14. *ApJ*, 543:340–350, 2000.

C. Thompson, M. Lyutikov, and S. Kulkarni. Electrodynamics of magnetars: Implications for the persistent x-ray emission and spin-down of the soft gamma repeaters and anomalous x-ray pulsars. *ApJ*, 574:332–355, 2002.

V. Urpin and D. Shalybkov. Effect of Hall currents on magnetic-field dissipation. *Sov. Phys. JETP*, 73:703–707, 1991.

S. I. Vainshtein, S. M. Chitre, and A. V. Olinto. Rapid dissipation of magnetic fields due to the Hall current. *Physical Review E*, 61:4422–4430, 2000.

D. Viganò, J. Pons, and J. Miralles. A new code for the Hall-driven magnetic evolution of neutron stars. *arXiv:1204.4707*, 2012.

C. Wareing and R. Hollerbach. Cascades in decaying three-dimensional electron magnetohydrodynamic turbulence. *Journal of Plasma Physics*, 76:117, 2010.